Performance Enhancement of Small-Scale Wind Turbine Featuring Morphing Blades

Md. Zishan Akhter[1], Ahmed Riyadh Ali[2], Hasan Kamliya Jawahar[3], Farag Khalifa Omar[1,#], Emad Elnajjar[1]

[1] Department of Mechanical & Aerospace Engineering, United Arab Emirates University, UAE,

Emails: 201990196@uaeu.ac.ae (MZA), fomar@uaeu.ac.ae (FKO), eelnajjar@uaeu.ac.ae (EE)

[2] School of Mechanical & Aerospace Engineering, Nanyang Technological University, Singapore,

Email: ahmedriy001@e.ntu.edu.sg

[3] Department of Mechanical Engineering, University of Bristol, UK,

Email: hasan.kj@bristol.ac.uk

Abstract

The demand for renewable energy is driven by the depletion and adverse environmental impacts of fossil fuels. There is a growing global consensus for research and development of renewable energy, including wind. In the current study, National Renewable Energy Laboratory (NREL) Phase VI wind turbine blade is integrated with morphing trailing-edge, installed on the aft-30% blade chord, across outboard 75% blade span. The morphing trailing-edge generates unique topology for each wind speed such that the glide ratio is maximized along the blade span. Three-dimensional transient computational fluid dynamics (CFD) analyses are conducted over low to medium wind speeds to investigate the blade aerodynamics. The analyses exhibit significant increments in the low-speed shaft torque and power of the morphed blades compared to the baseline. The integration of morphing trailing-edge high-lift flow control mechanism on the NREL Phase VI blade enhanced energy harvesting and reduced the wind turbine cut-in wind speed. Comparative investigations are also conducted to assess the improvements in thrust, bending moment, and aerodynamic load distribution, as well as alterations in the pressure, flow field, turbulence, surface flow, and wake. The aeroacoustics directivity of the wind turbines exhibits marginal far-field noise increment in case of morphing trailing-edge integrated blades.

Keywords: wind turbine, morphing trailing-edge, flow control, turbulence, far-field noise

[#] Corresponding Author.
Email address: fomar@uaeu.ac.ae (F. K. Omar)

Nomenclature

C -	blade chord (m)
R -	blade span (m)
x/C -	chord fraction
r/R -	span fraction
D -	wind turbine diameter (m)
H -	hub height (m)
U_w -	wind speed (m/s)
C_P -	power coefficient
C_{prs} -	pressure coefficient
C_L -	lift coefficient
C_D -	drag coefficient
C_L/C_D -	lift-to-drag ratio
λ -	tip speed ratio
α -	angle of attack (°)
β -	trailing-edge (MTE) deflection (°)
f -	frequency (Hz)
SS -	Suction surface
PS -	Pressure surface

1. Introduction

There is a growing consensus to phase out carbon-intensive energy sources in favor of environmentally friendly, sustainable alternatives such as solar, wind, hydro, wave, geothermal, and biogas. Wind energy has gained popularity due to its technological maturity and cost-effectiveness. As of 2021, wind energy generated 27% of the net Global Renewable Energy (GRE) production [1]. Small-scale horizontal axis wind turbines, with rotor diameters of up to 20m and power ratings of up to 100kW, are becoming popular as independent power sources. They are more affordable and have lower operating and maintenance costs, making them a reliable option for off-grid rural and suburban areas [2,3]. They are also suitable for areas with low wind potential [4,5], such as sub-Saharan Africa where 77% of the global population without access to electricity lives [6]. Small-scale wind turbines present a viable and attractive renewable energy solution for achieving Sustainable Development Goal (SDG 7) which aims to ensure access to clean and affordable energy [6]. However, their commercial success depends on economic feasibility of generated power, which is determined by initial cost per watt of power and unit cost per kWh [7].

Blade design and optimization is a major focus of research in academia and industry [8,9]. Researchers have developed various mechanisms for controlling flow transition/separation and managing turbulence on/around the blades to enhance the aerodynamic performance and load stability of wind turbines [10]. These mechanisms can be broadly classified into active and passive control techniques. Passive techniques involve installation of microstructures, such as vortex generators [11], winglets [12], slats [13–16], riblets [17], surface texture/roughness [18], and slot/dimples/grooves [19], which manipulate pressure gradient across the blade surface to improve flow characteristics and aerodynamic performance. Active flow control mechanisms use a network of microsensors installed across the blade surface, which actively process sensor feedback to maintain or achieve optimal aerodynamic response through necessary local actuations [10,20]. Popular active control devices include flaps [21–30], plasma actuators [31], blowing/suction [32], and blade chord/camber/span/twist morphing [33–38], among others. Passive control techniques are characterized by simple structure, low cost, and easy implementation, but they offer a narrow adaptation range and poor regulation performance. Active techniques, on the other hand, offer greater flow control flexibility but require a small range of external energy input.

Conventional high-lift devices such as flaps manipulate the effective camber of a wing/blade to regulate aerodynamic forces by altering the chordwise pressure distribution [39]. However, these discrete control surfaces have several disadvantages, including exposure to wear and corrosion, high costs, weight penalties, increased aerodynamic drag, and aeroacoustic noise. Numerous structural morphing concepts have been developed as efficient alternatives to provide seamless, smooth, gradual changes in the contour to enhance flow control while minimizing inherent aerodynamic losses, noise, and structural vibration [40]. Several review articles have focused on innovative morphing technologies for use in aerospace [40–42], wind turbines [10,33,43], and helicopter rotors [44,45]. Morphing trailing-edge flaps are among the most effective flow control mechanism for wind turbines [46,47]. They effectively tailor the aerodynamic response of wind turbines under a range of steady and unsteady wind conditions, providing relative increments of up to 0.13 in the lift coefficient and nearly 80% reduction in lift fluctuation [48,49]. They have also been used for load alleviation [50,51] and stall control [52,53], resulting in up to a 13% reduction in blade-root bending moment [54] and up to a 15% reduction in extreme and fatigue loads on the shaft, nacelle, and tower [55].

Most previous research on morphing trailing-edges (MTE) has focused on large-scale turbines for load control and regulation. However, the design and application of MTE for power augmentation in small-scale turbines is a research area yet to be fully investigated. In previous work [56–58], the authors successfully demonstrated the significance of MTE in maximizing energy extraction. They designed and developed a trailing-edge morphing module integrated across the outboard 70-85% blade span of a small-scale wind turbine, demonstrating up to 53 % power augmentations. The current research aims to further explore the potential of MTE in small-scale wind turbines, specifically in lowering the cut-in wind speed and increasing the start-up torque. This holds the potential to significantly increase annual energy production (AEP) and reduce the levelized cost of energy (LCOE) of the wind turbines. An NREL Phase VI wind turbine is equipped with MTE across the outboard 75% blade span to evaluate the subsequent performance enhancement and power augmentation.

2. Blade and Morphing Trailing-edge Design

2.1 Baseline Wind Turbine

This study focuses on a National Renewable Energy Laboratory (NREL) Phase VI research wind turbine, shown in Fig. 1 [59]. It is a two-bladed, fixed-pitch, stall-regulated, horizontal axis wind turbine operated in an upwind configuration. The design, components, and operating parameters of the wind turbine are detailed in Table 1. The aerodynamic analysis in this research uses the NREL Phase VI (Experiment: Sequence H) blade as the benchmark. This blade is referred to as the "Baseline blade" in the following text. The three-dimensional CAD model of the baseline blade is shown in Fig. 2. It has a linearly tapered and twisted planform, which is shown in Fig. 3. The blade has a span of $R = 5.029$ m, measured from the wind turbine hub center at $r = 0$ m. The blade's cylindrical root spans $0.508 \text{ m} \leq r \leq 0.883$ m, transitioning into the S809 airfoil at $r = 1.257$ m. The blade planform beyond this point, $1.257 \text{ m} \leq r \leq 5.029$ m, features the S809 airfoil contour. Flatback airfoils are commonly used in design and production due to their aerodynamic, structural, and manufacturing feasibility. Therefore, it should be noted that the blades modeled in this research have trimmed trailing-edges equivalent to 0.5% of the sectional chord length.

2.2 Morphing Trailing-Edge Design

The NREL Phase VI wind turbine blades are shaped by the S809 airfoil. To create a morphing trailing-edge, the aft-30% chord region of the S809 airfoil is modified geometrically. The proposed morphing trailing-edge features a smooth, seamless camber deflection, based on the author's previous research in Ref. [34,35,60,61]. The morphing

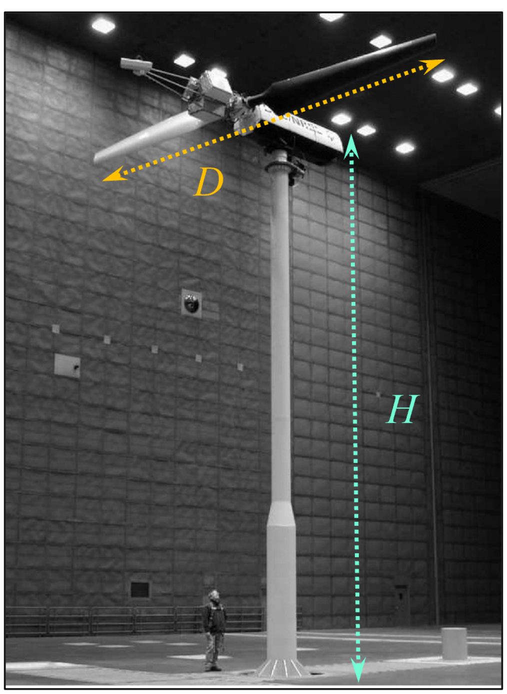

Fig. 1.: NREL Phase-VI wind turbine [59]

Table 1: Design and operating parameters of NREL Phase-VI wind turbine.

NREL Phase-VI Wind turbine	
Number of blades	2
Wind turbine diameter (D)	10.06 m
Hub height (H)	12.2 m
RPM	72
Cut-in wind speed	5 m/s ($\lambda = 7.6$)
Rated wind speed	13.5 m/s
Cut-out wind speed	25 m/s ($\lambda = 3.3$)
Rated power	19.8 kW
Cone angle	0°
Blade tip pitch angle	3°
Blade profile	S809
Blade chord (C)	(0.358-0.737) m
Blade thickness (t/C)	21%

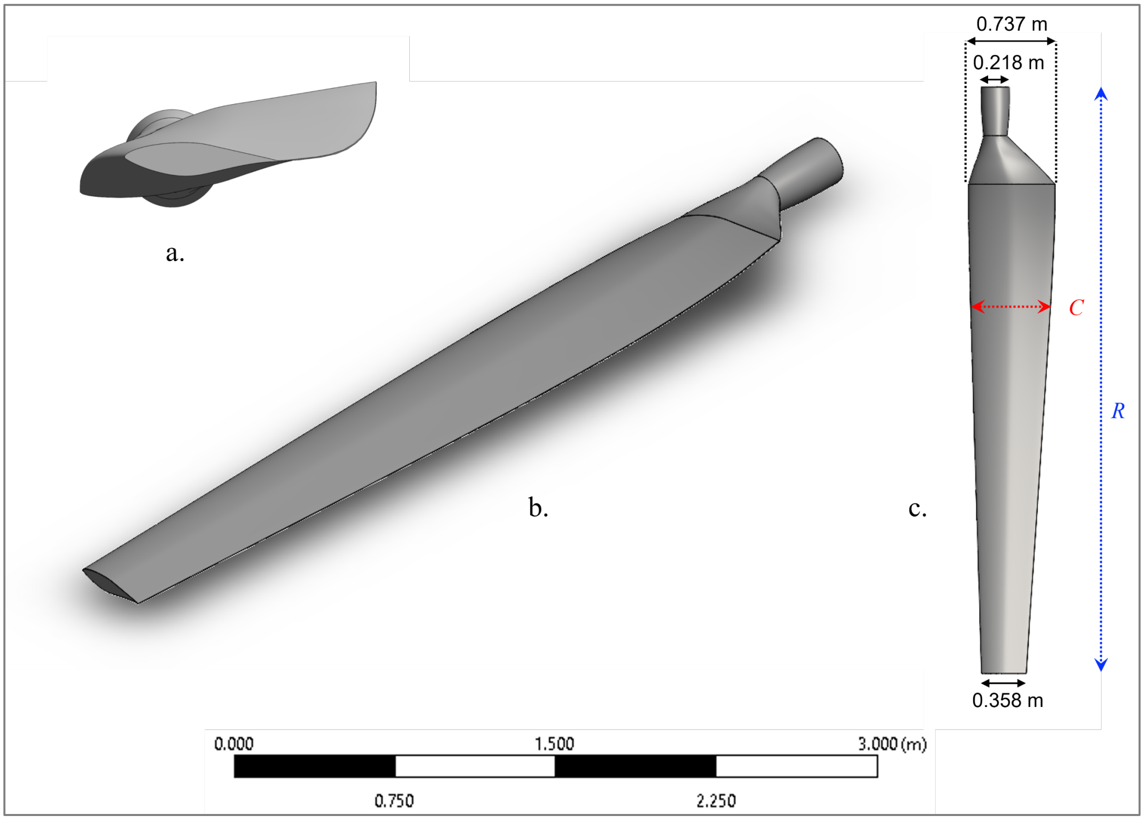

Fig. 2: NREL Phase-VI wind turbine blade: (a) cross-view, (b) iso-view, and (c) top-view.

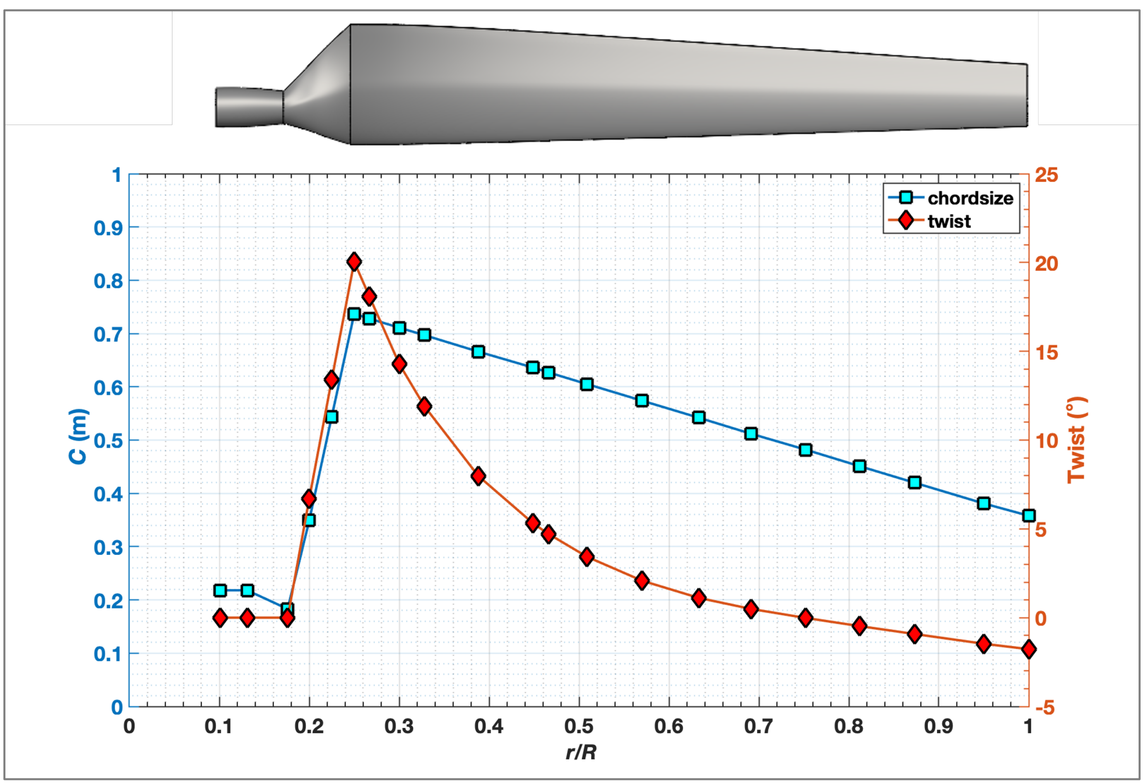

Fig. 3: Geometric design of NREL Phase VI Baseline blade.

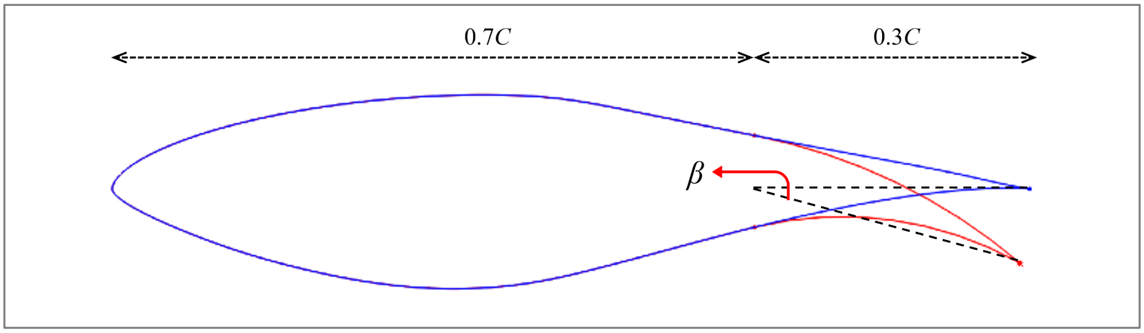

Fig. 4: Schematic of S809 morphing airfoil (blue), integrated with (red) morphing trailing-edge (MTE).

trailing-edge deflection angle (β) is defined as the angle formed by the intersection of the deflected chord line with the original at the 70% chord length from the leading-edge, as shown in Fig. 4.

A comprehensive parametric study is conducted to determine the optimal trailing-edge topology based on varying flow conditions. The design optimization is performed with the objective to maximize lift (C_L) while minimizing drag (C_D) increment, resulting in a maximized lift-to-drag ratio (C_L/C_D) achievable through trailing-edge morphing. This is accomplished by modeling fifteen S809 airfoils, each with a chord size (C) of 0.305 m and span of 0.01C. Each airfoil model featured a unique trailing-edge deflection angle, ranging from β = 0° (baseline) to β = 15°. In order to determine the ideal trailing-edge deflection angle (β) for achieving the highest lift-to-drag ratio (C_L/C_D) at each incidence angle (α), the models are subjected to a range of angles of attack, α = -6° - 20°. The selected range of angles of attack (α) is carefully determined based on the variation in the inflow angles of attack across the blade span with the windspeed.

The simulations are performed using the k-ω Shear Stress Transport turbulence model and a coupled pressure-based algorithm with a least-square cell-based scheme and second-order discretization. The numerical modeling used in this study is adapted from the author's previous work in Ref. [61]. The CFD simulations are conducted at a uniform inflow of 50 m/s, corresponding to chord-based Reynolds number of 1 million.

The performance of the morphing airfoils is compared to that of the conventional S809 airfoil. The results showed that the morphing airfoils exhibited a significant improvement in C_L/C_D, particularly at angles of attack of $\alpha \leq 10°$. The highest C_L/C_D ratio exhibited by designed morphing airfoils over the tested angles of attack (α), is plotted against the conventional airfoil in Fig. 5. The relative C_L/C_D enhancements achieved by the morphing airfoils are summarized in Table 2.

The Baseline blade is divided into small sections based on design data from the literature [59]. Each section, ranging from 0.25 ≤ r/R ≤ 1.0, is treated as a three-dimensional S809 airfoil. The trailing-edges of these sections are optimized to maximize the lift-to-drag ratio (C_L/C_D) based on the incoming angles of attack (α). As a result, four unique blades with morphing trailing-edges (referred to as "MTE blades") are designed for the tested wind speeds of U_w = 3, 5, 7, and 9 m/s. The spanwise morphing of the generated MTE blades is shown in Fig. 6. The MTE blades are labeled "MX", where M indicates a morphing trailing-edge and X specifies the corresponding wind speed.

3. Computational Fluid Dynamics Modeling

In this study, the commercial Ansys Fluent Solver is used for numerical modeling and analysis. The specific turbulence model, computational domain and grid, boundary conditions, and solver settings employed in the Computational Fluid Dynamics (CFD) analyses are described in this section.

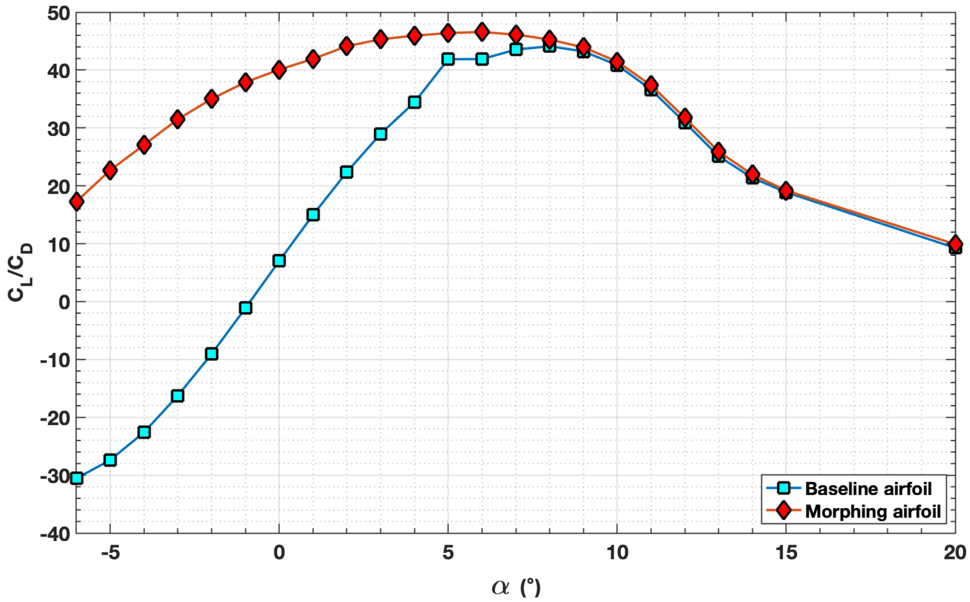

Fig. 5: Glide ratio performance of S809: Baseline, and Morphing airfoils.

Table 2: Maximum relative glide ratio enhancements achieved through various MTE deflections (β), over tested angles of attack (α).

Angle of Attack (α)	MTE deflection (β)	Relative enhancement $\Delta(C_L/C_D)$
-6°	15°	157%
-5°	15°	183%
-4°	13°	220%
-3°	13°	294%
-2°	12°	487%
-1°	11°	3453%
0°	11°	471%
1°	10°	180%
2°	8°	97%
3°	8°	56%
4°	6°	33%
5°	5°	11%
6°	4°	11%
7°	3°	6%
8°	2°	3%
9°	1°	2%
10°	1°	1%
11°	1°	2%
12°	1°	3%
13°	1°	3%
14°	1°	3%
15°	1°	2%
20°	1°	7%

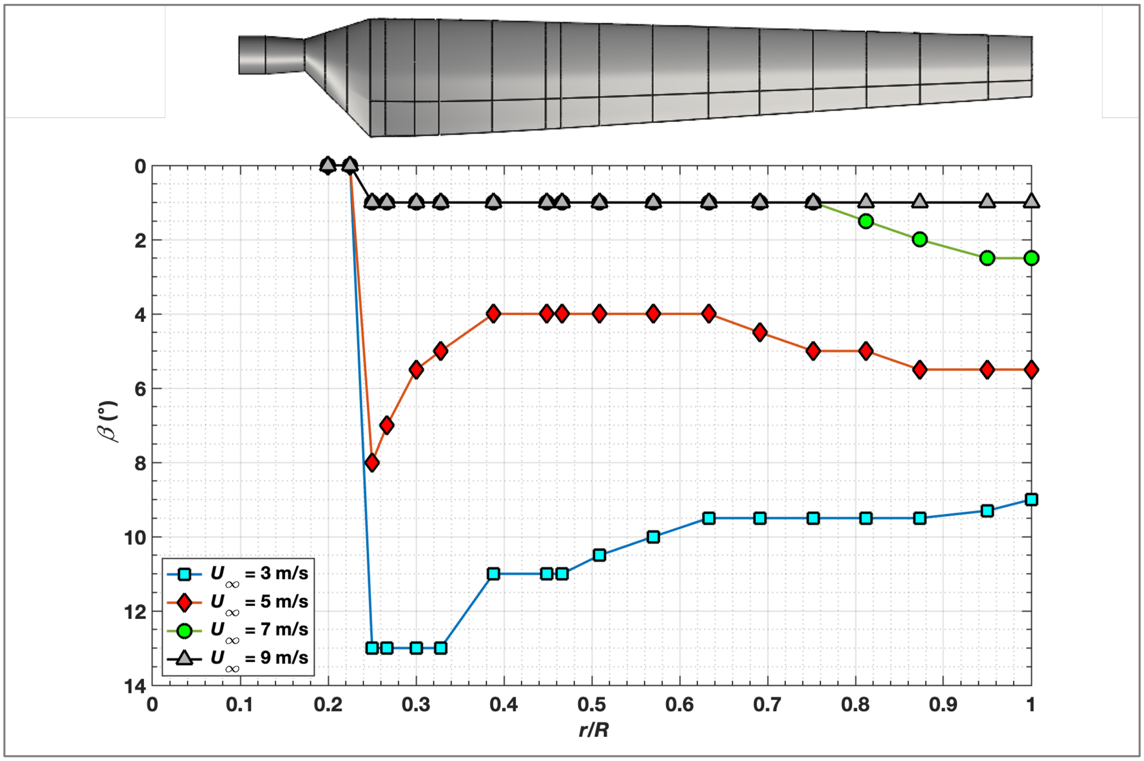

Fig. 6: Optimized trailing-edge deflection (β) of the NREL Phase-VI MTE blades for different wind speeds.

3.1 Turbulence Modeling

The CFD analysis involves the application of the Navier-Stokes Equations (NSEs), a set of partial differential equations that describe the fundamental physical laws of conservation of mass, momentum, and energy [62]. To solve these equations, the computational domain is divided into smaller finite-volume elements, and the equations are numerically approximated using discretization techniques. The local solutions obtained from each element are then iteratively combined to obtain a global solution.

In this research, the Menter's two-equation eddy-viscosity Shear Stress Transport (SST) k-ω model is used for its accuracy and reliability in predicting external flows in various aerodynamic applications. This hybrid model combines the k-ε and standard k-ω models, and can switch between them in order to provide robust computations across the domain, from the far-field freestreams to the near-wall viscous sublayers. The SST k-ω model is particularly useful in predicting adverse pressure gradients, flow transitions, free shear flows, and boundary layer dynamics [63,64], making it a popular choice in wind turbine aerodynamics research for its ability to accurately model flow transitions and stall phenomena [65–69].

The SST *k-ω* model formulates the conservation of mass, and momentum, in conjunction with the transport of-turbulence kinetic energy, and specific dissipation, through Eqs. (1)-(4), as follows:

$$\frac{\partial \bar{u}_i}{\partial x_i} = 0 \quad (1)$$

$$r\bar{u}_j \frac{\partial \bar{u}_i}{\partial t} = r\bar{f}_i + \frac{\partial}{\partial x_j}\left[-\bar{p}\delta_{ij} + 2m\bar{S}_{ij} - r\overline{u_i'u_j'}\right] \quad (2)$$

$$\frac{\partial}{\partial t}(\rho k) + \frac{\partial}{\partial x_j}(\rho u_j k) = P - \beta^* \rho \omega k + \frac{\partial}{\partial x_j}\left[(\mu + \sigma_k \mu_t)\frac{\partial}{\partial x_j}(k)\right] \quad (3)$$

$$\frac{\partial}{\partial t}(\rho \omega) + \frac{\partial}{\partial x_j}(\rho u_j \omega) = \frac{\gamma}{\nu_t}P - \beta \rho \omega^2 + \frac{\partial}{\partial x_j}\left[(\mu + \sigma_\omega \mu_t)\frac{\partial}{\partial x_j}(\omega)\right] + 2(1 - F_1)\sigma_{\omega^2}\frac{\rho}{\omega}\frac{\partial}{\partial x_j}(k)\frac{\partial}{\partial x_j}(\omega) \quad (4)$$

where, u represents the velocity vector, μ_t denotes turbulent eddy viscosity, r denotes fluid density, $\bar{p}$ denotes pressure, S indicates strain tensor, and ω symbolizes specific dissipation.

3.2 Computational Domain and Grid

The NREL Phase VI wind turbine used in this study has a two-bladed configuration with rotational symmetry around the hub. This offers the scope to model just one blade for significant grid size and computational expense reduction by utilizing 180° periodicities. The aerodynamic interactions of the tower and nacelle are not included in this study for simplicity. The computational domain used has a semi-cylindrical geometry extending 25 meters ($5R$) upstream and 50 meters ($10R$) downstream of the blade, with radii of 0.5 meters ($0.1R$) and 25 meters ($5R$) at the semi-cylindrical frictionless walls serving as the Virtual Wall and Symmetry, respectively. The domain features two axisymmetric sub-domains to accurately capture the near- and far- field flow dynamics. The dimensions and boundary conditions of the computational domain are shown in Fig. 7. These boundaries are placed sufficiently far to avoid any wall effects on the near-field computations, and prevent the backflow anomaly [68].

The computational domain is used to generate high-resolution hexahedral mesh using Ansys ICEM software. The preliminary mesh is designed with 35 inflation layers normal to the blade surface to precisely capture the boundary layer dynamics. The first-cell height is adjusted to 0.02 mm, in order to fulfill the non-dimensional wall-distance criterion of ($Y^+ < 1$), proposed for SST *k-ω* model [66]. The meshing scheme used for high-resolution grid generation is adopted from author's previous work in Ref. [58]. The control volume grid is presented in Fig. 8, along with close-ups of the blade tip, and surface meshing.

3.3 Boundary Conditions and Solver Settings

In this research, the Single Reference Frame (SRF) methodology is used for numerical analysis. This approach assigns the angular speed of the wind turbine to the reference frame while modeling the surrounding flow field as a steady entity [70]. The boundary conditions used in the simulations, shown in Fig. 7, have been found to be effective in previous studies [58,68,69]. The governing Unsteady Reynolds-averaged Navier–Stokes (URANS) equations and the SST k-ω transport equations are solved using a pressure-based coupled scheme, which allows for faster convergence by treating the continuity, momentum, and transport equations as a coupled system [71]. The spatial discretization for cell face value interpolation is performed using a second-order Upwind scheme, while cell gradient and secondary diffusion terms are calculated using a least-square cell-based scheme. A second-order implicit scheme is used for temporal discretization to achieve stability at larger timesteps by avoiding inherent Courant–Friedrichs–Lewy (CFL) constraints. The simulation period in this study is approximately 1.68 seconds, representing two rotational cycles of the NREL Phase VI wind turbine. The transient timestep size is 0.003 seconds, performing a minimum of 30 iterations/timestep. A convergence criterion of 10^{-5} is used to monitor the normalized scaled residuals. Finally, the aerodynamic results are computed by averaging the values obtained over the final 500 timesteps (approximately 15000 iterations) of the simulation [69].

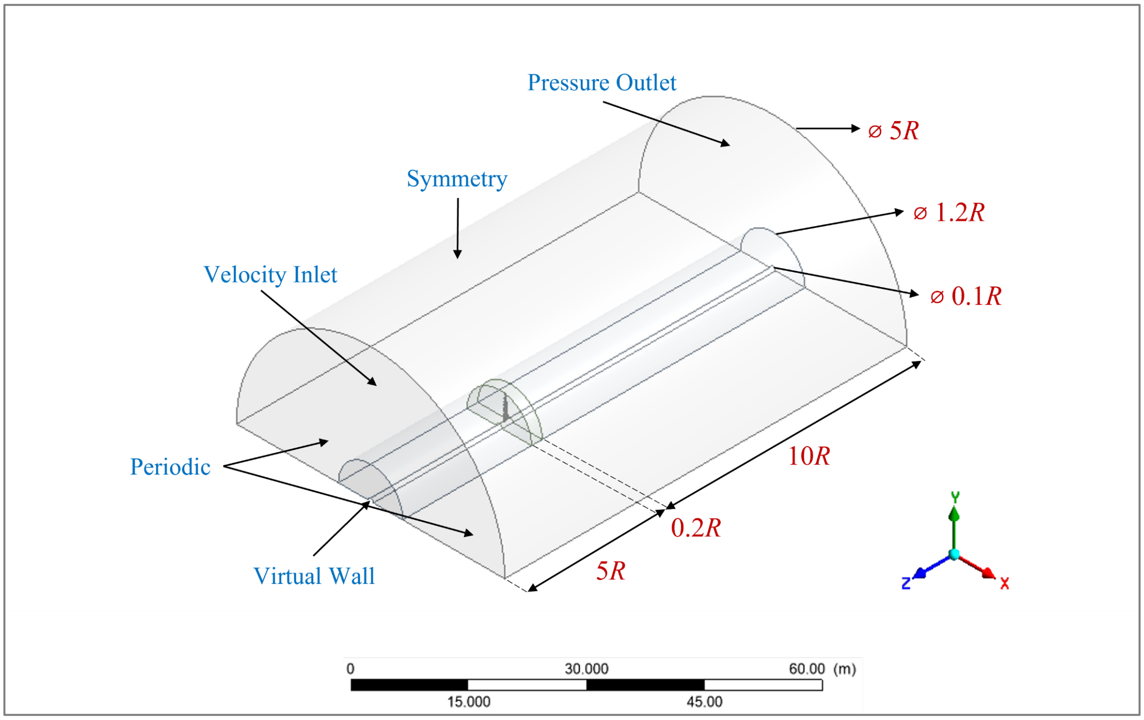

Fig. 7: Computational domain and boundary conditions used in CFD modeling [flow direction: -z axis].

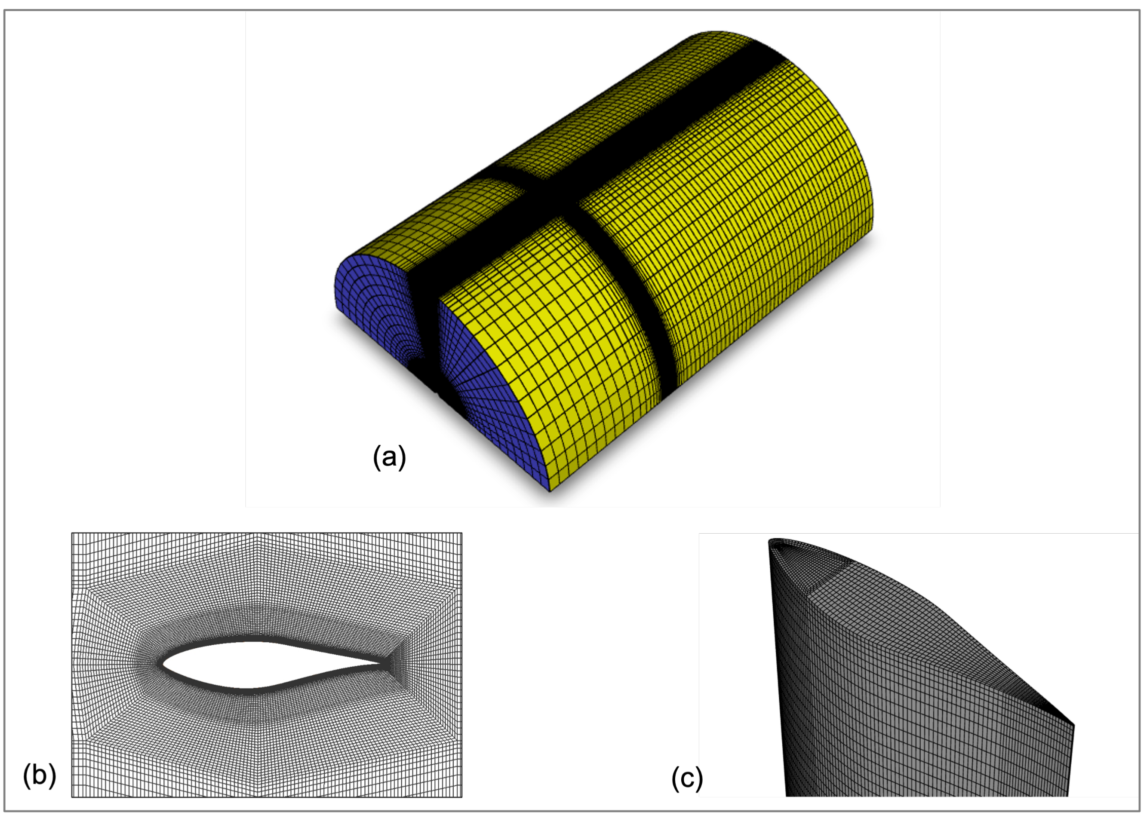

Fig. 8: CFD mesh: (a) control volume grid, (b) blade-tip mesh close-up, and (c) blade surface mesh.

3.4 Mesh sensitivity analysis

A grid independence study is conducted to ensure that the results are not influenced by the mesh resolution. Four meshes of progressively increasing resolution are tested, as summarized in Table 3. The convergence test is performed for a range of wind speeds (U_w = 5-9 m/s) to verify the accuracy and reliability of the aerodynamic predictions at different tip speed ratios (λ). The performance of the grid is evaluated by comparing the Coefficient of Power (C_P) obtained for the different wind speeds. As shown in Fig. 9, the C_P predictions from the different meshes diverge slightly at higher wind speeds (lower tip speed ratios). The C_P results from the Fine and Ultra-fine grids differ by ≤ 0.4% over the tested range. Therefore, the Fine grid (11 million cells) is selected for this research to achieve the necessary precision at a reasonable computational cost.

Table 3: Detailed parameters of tested NREL Phase-VI wind turbine grids.

Parameters	Coarse Grid	Medium Grid	Fine Grid	Ultra-fine Grid
Wrap-around nodes	114	230	348	460
Leading edge nodes	8	15	23	25
Trailing-edge nodes	8	15	23	25
First-layer height (m)	2×10^{-5}	2×10^{-5}	2×10^{-5}	2×10^{-5}
Growth rate	1.2	1.2	1.2	1.2
Total Cells	4.5×10^6	7.7×10^6	11.0×10^6	14.3×10^6

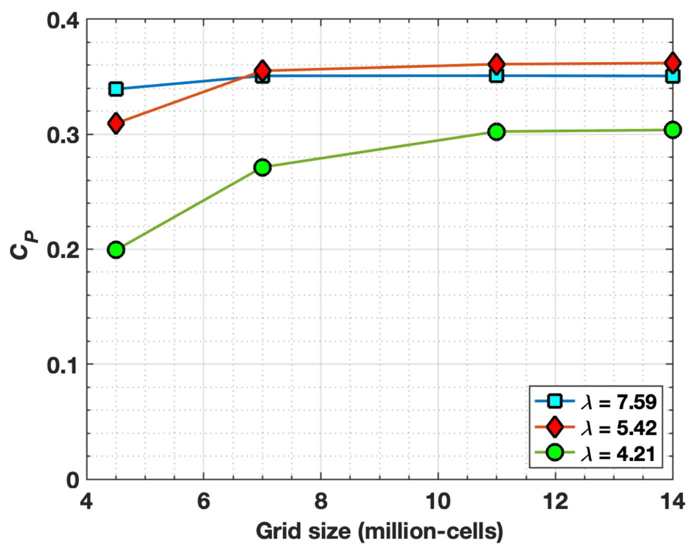

Fig. 9: Grid sensitivity analysis using four meshes of sequentially increasing size: (4.5-14.3) million cells.

3.5 Aeroacoustics

The outboard region of wind turbine blades, spanning from $0.75 \leq r/R \leq 0.95$ of the blade radius, is known to be the primary source of noise, owing to high local inflow velocities [72]. Whereas the dominant noise sources within blade regions of $r/R \leq 0.75$ are associated with frequency of $f < 1$ kHz, and thus, can be neglected while modelling noise disturbance. In this research, the noise generated by the NREL Phase-VI blades is simulated in the outboard region using the Large Eddy Simulation (LES) model and the Ffowcs-Williams and Hawkings (FW–H) acoustic analogy. The simulations use a transient timestep size of 1 x 10^{-6} seconds to satisfy the condition of CFL < 1, for a total duration of 0.075 seconds simulating 35 degrees of blade rotation which is sufficient for wind turbine noise prediction [73]. The acoustic computations are performed using a dense grid of approximately 11 million hexahedral cells, as shown in Fig. 10. The domain size and boundary conditions are referred from the literature featuring wind turbine computational aeroacoustics [73]. The dimensions of the annular domain are normalized with the blade span and tip chord.

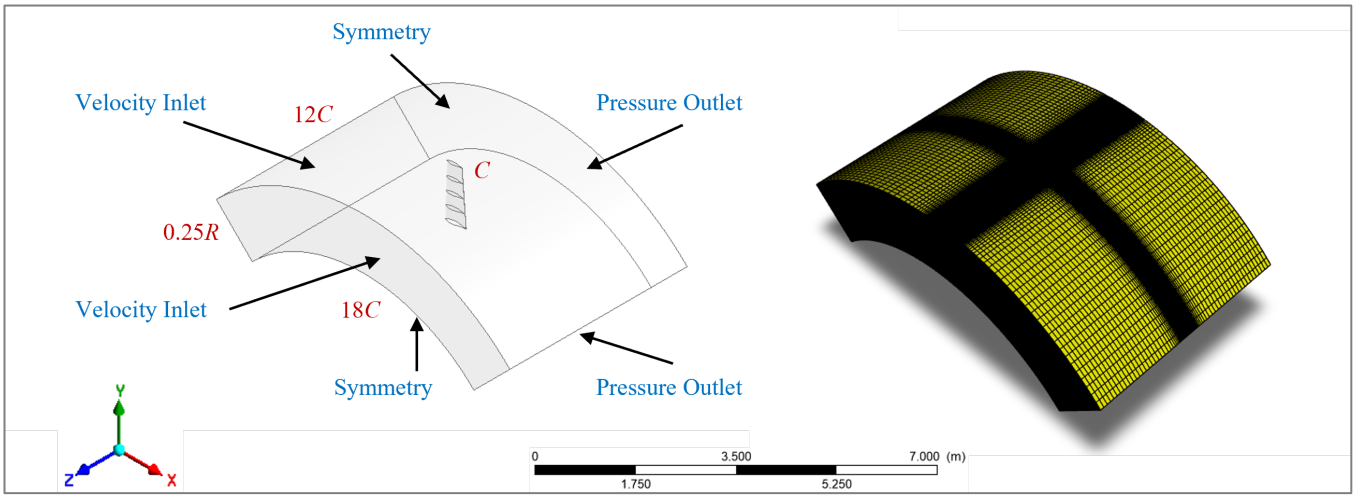

(a) **(b)**

Fig. 10: Computational Aeroacoustics (CAA) modeling: (a) domain and boundary conditions, (b) structured LES grid. [flow direction: -z axis]

4. Results

4.1 Model Validation

The reliability and accuracy of the CFD modeling is evaluated by comparing the computed predictions with experimental data from the literature [59]. The results for the Baseline blade are obtained for a wind speed range of U_w = 5-13 m/s, which corresponds to a tip speed ratio range of λ = 2.9-7.6. This range is chosen to assess the accuracy of the computational model in simulating blade aerodynamics over the pre-stall to stalled flow conditions. The CFD model used in this study accurately predicts the low-speed shaft torque and power over the tested wind speed range, with a relative error of ≤ 5.5%. The power coefficient (C_P) of the Baseline blade, shown in Fig. 11, is in good agreement with the experimental results. Additionally, the CFD results are validated by comparing the computed pressure distribution on the blade surface with the experimental results at five span stations (r/R = 0.30, 0.47, 0.63, 0.80, 0.95) for two wind speeds (U_w = 5 and 9 m/s). The corresponding pressure coefficients for the Baseline blade also demonstrate good agreement with the experimental results (refer supplementary data).

4.2 Torque and Power

The numerical analysis of the modeled NREL Phase-VI Baseline and MTE blades were analyzed for low-speed shaft torque and resulting power generation over a wind speed range of 3-9 m/s, corresponding to tip speed ratios of λ = 12.6-4.2, respectively. The superiority of the MTE blades, particularly at low wind speeds, is evident from the detailed comparative analysis in Table 4. The MTE blades show torque and power increments of up to 103.8 N.m and 0.8 kW, respectively, at a wind speed of 5 m/s, corresponding to a relative increase of 39.9%. Additionally, the power coefficient (C_P) of the simulated models is evaluated, with the MTE blades demonstrating higher efficiency in power generation than the Baseline blade. The comparative C_P plots in Fig. 12 show relative enhancements for the MTE blades at all tested wind speeds. The maximum C_P increase of 0.14 is achieved by the MTE blades at a wind speed of 5 m/s (λ = 7.6), corresponding to a 39.9 % relative increase. It is worth noting that the MTE blades significantly reduce the cut-in wind speed to 3 m/s, exhibiting torque increment of up to 600% and generating 0.55 kW of power, thereby boosting the wind turbine AEP and overall productivity.

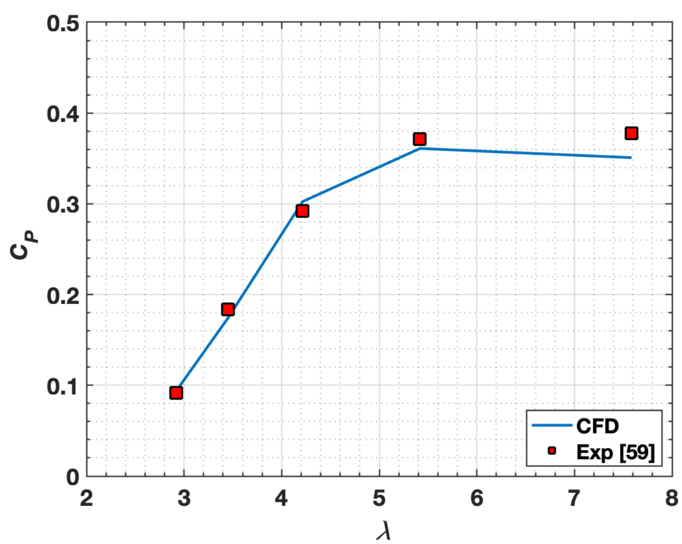

Fig. 11: Computational validation of NREL Phase-VI Baseline blade through power coefficient (C_P) prediction.

Table 4: Torque and Power variation of the NREL Phase-VI: Baseline, and MTE blades.

Wind speed, U_w (m/s)	Tip Speed Ratio (λ)	Torque (N.m)		Power (kW)		Relative Increment
		Baseline	MTE	Baseline	MTE	
3	12.6	10.48	73.4	-	0.55	600.4%[#]
5	7.6	260.02	363.82	1.96	2.74	39.9%
7	5.4	734.18	789	5.54	5.95	7.5%
9	4.2	1307.22	1396.14	9.86	10.53	6.8%

[#] The relative increment is computed for torque, as there is no power generation for the Baseline at 3 m/s wind speed.

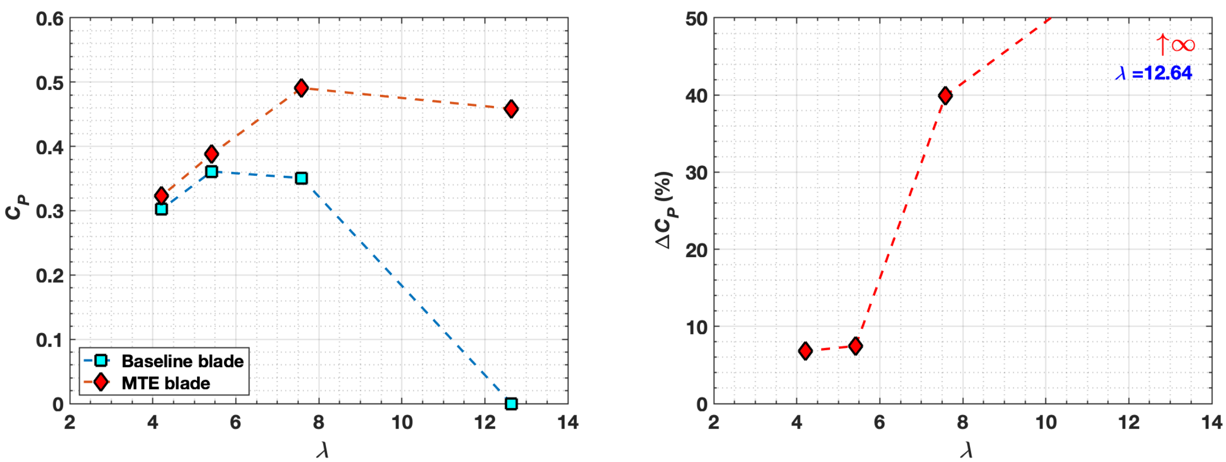

(a) **(b)**

Fig. 12: Performance variation of NREL Phase-VI: Baseline, and MTE blades, exhibiting (a) Coefficient of power (C_P), and (b) relative increment in power coefficient (ΔC_P), with respect to tip speed ratio (λ).

To investigate the impact of trailing-edge morphing on wind turbine performance, the torque distribution is analyzed along the blade span in Fig. 13. The results present a similar overall trend for both blades with increasing wind speed. The torque steadily increases along the inboard sections, reaching a peak near the r/R = 0.8 span station, before gradually decreasing over the outboard span stations (r/R > 0.8) with a sharp drop near the blade tip (r/R > 0.95). The MTE blades show significant torque increments across the entire blade span compared to the corresponding Baseline blade, with relative increments up to (157, 226, 111)%, (70, 43, 9)%, (10, 9, 6)%, and (12, 5, 3)%, at the blade span stations of r/R = 0.29, 0.83, and 0.98 for wind speeds of 3, 5, 7, and 9 m/s respectively. It is noteworthy that at a wind speed of 3 m/s (λ = 12.6), the Baseline blade produces driving torque only over the outboard half-span ($r/R \geq 0.5$). The inboard sections of the Baseline blade exhibit negative torque values due to negative local angles of attack (α), as detailed in the upcoming sections. In contrast, the MTE blades produce favorable torque over the entire span, resulting in an increase in the power coefficient and a reduction in the cut-in wind speed. The sectional torque analysis in Fig. 14 shows that Region II ($0.63 \leq r/R \leq 0.81$) is the most favorable zone for the enactment of trailing-edge morphing on the Baseline blade to increase power output. It is followed by Regions I ($0.81 \leq r/R \leq 1.0$), III ($0.44 \leq r/R \leq 0.63$) and IV ($0.25 \leq r/R \leq 0.44$), in terms of torque contributions.

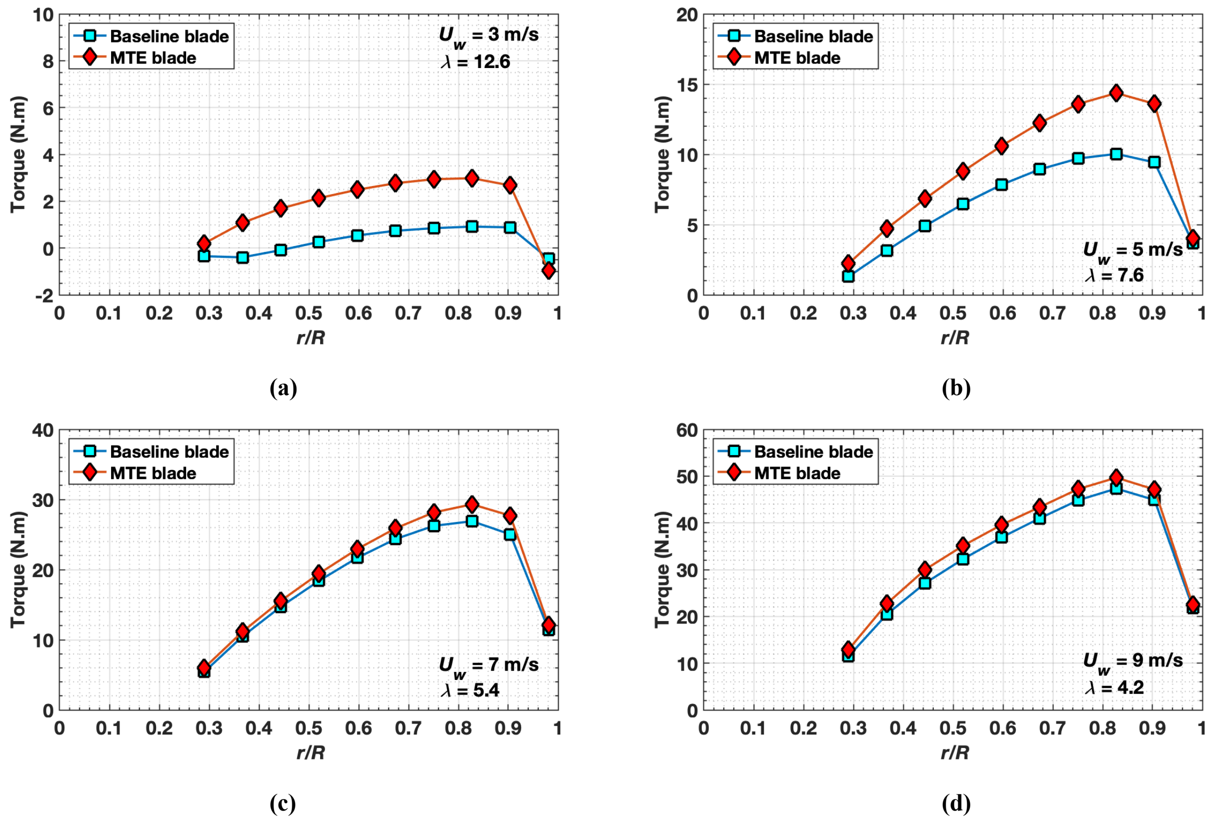

Fig. 13: Spanwise distribution of Torque, of NREL Phase-VI: Baseline, and MTE blades.

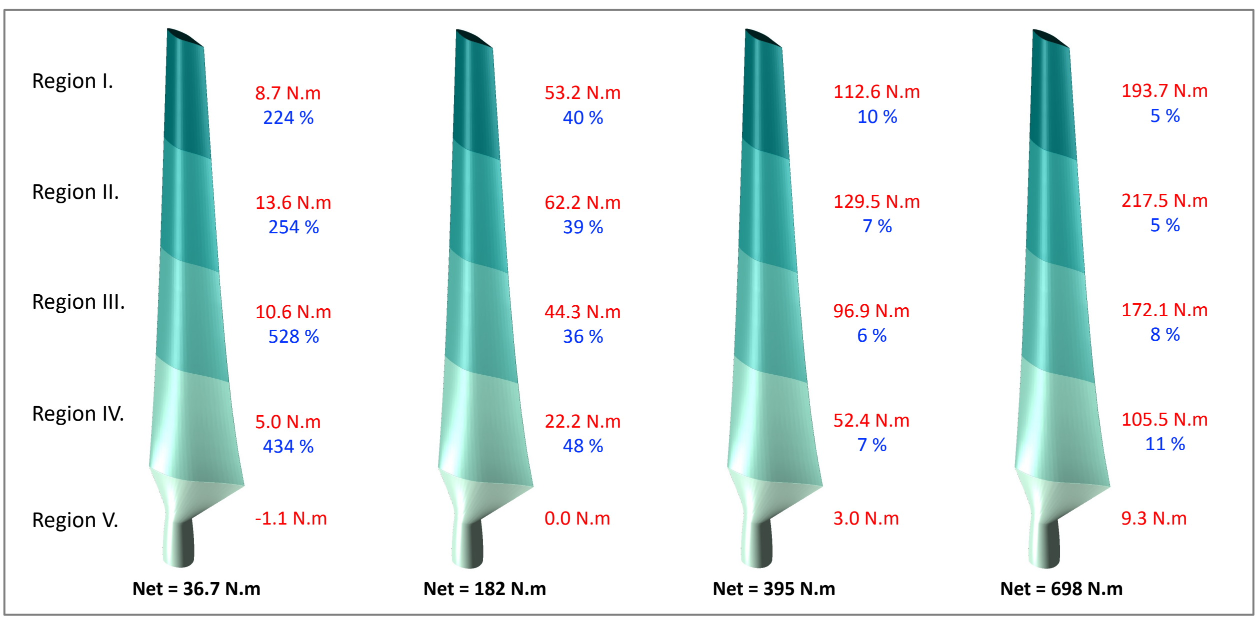

(a) M3 **(b) M5** **(c) M7** **(d) M9**

Fig. 14: Torque generation over different sections of MTE Blades presenting: (red) regional torque contribution, and (blue) relative increment (%) compared to the Baseline.

4.3 Thrust and Flap Bending Moment

During operation, wind turbines are subjected to axially moving inflow which generates thrust force on the blades. This force results in concentrated stresses at the blade root, known as flapwise bending moment. These parameters indicate the amount of kinetic energy harnessed by the blades from the incoming wind. The thrust force and resulting flapwise bending moment are calculated for the wind speed range of 3-9 m/s. A detailed comparison is provided in Table 5. As expected, the thrust force and bending moment on the blades increase with wind speed due to the increase in inherent kinetic energy at higher speeds. The MTE blades experience relatively larger thrust force and resulting bending moment, as seen in Fig. 15. The increments in thrust and bending moment are up to 140 N (45.8%) and 505 N·m (47.6%) respectively, at a wind speed of 5 m/s. At the reduced cut-in wind speed of 3 m/s, the MTE blades experience 367% and 325% increments in the thrust and flapwise bending moment, respectively. This is largely attributed to the blade camber enlargements achieved through trailing-edge morphing.

The effect of trailing-edge morphing on blade aerodynamics is further analyzed through spanwise thrust assessment. The load distributions for the blades exhibit a similar trend with increasing wind speed, as depicted in Fig. 15. The thrust force steadily increases across the inboard regions, with maxima observed at span stations $0.8 \leq r/R \leq 0.9$. This is followed by a sharp decrease in the thrust force in the outboard tip region of $r/R > 0.9$. The MTE blades demonstrate relatively higher thrust forces across the entire blade span for all tested wind speeds. The relative increments in thrust are recorded up to- (210, 273, 263)%, (66, 57, 67)%, (10, 14, 18)%, and (15, 6, 6)%, at the blade span stations of r/R = 0.29, 0.9, and 0.98, for wind speeds 3, 5, 7, and 9 m/s (λ = 12.6, 7.6, 5.4, and 4.2), respectively.

4.4 Pressure and Flow Field

In order to better understand the flow dynamics of the blades, pressure and flow visualization are conducted at five span stations, r/R = 0.30, 0.47, 0.63, 0.80, 0.95, across the simulated models, for a wind speed range of 3-9 m/s. Pressure coefficient contours with velocity streamlines are presented in Fig. 17-18 for only two wind speeds of U_w = 3 and 9 m/s, to maintain brevity. The results showed that the MTE blades, which have a modified trailing-edge topology, exhibit larger pressure gradients across the surfaces compared to the Baseline blade. The contours in Fig. 17-18 reveal increment in the pressure gradient with the buildup of larger negative and positive pressure zones on the suction and pressure surfaces of the MTE blades, respectively. This is attributed to the increased mean camber of the respective blade sections. Additionally, the MTE blades showed a decrease in the pressure coefficient suction-peaks by up to 534%, 279%, 3%, and 7% for wind speeds of 3, 5, 7, and 9 m/s, respectively. The pressure coefficient (C_{prs}) distribution around the Baseline and MTE blades are presented in Fig. 19. The exhibition is limited to span stations showcasing maximum C_{prs} relative enhancements, subject to the tested wind speeds. It is to be noted that the suction-surface C_{prs}-peak traverses from the leading-edge to mid-chord region under the influence of highly cambered profile of the MTE blades at lower wind speeds of 3 and 5 m/s. The C_{prs} distribution is synonymous with the C_{prs} contours provided in Fig. 17-18. These results correspond with the observed increment in torque and power output seen in the previous section.

The inherent blade twist and inflow Reynolds number variation, both contribute to the increase in local angle of attack (α) towards the blade root. The local incidence angles across the blade span $0.25 \leq r/R \leq 1.0$ range from α = (-7.3-1.5)°, (2.9-6.3)°, (7.4-12.6)°, and (10.3-19.2)° for wind speeds of U_w = 3, 5, 7, and 9 m/s, respectively. This increase in local angles of attack modifies the flow behavior across different span stations of the blades. At wind speeds of 3, 5, and 7 m/s, the blades experience attached flow, however, at a wind speed of 9 m/s, the Baseline and MTE blades experience flow transition and separation over the midspan region due to the increase in local angles of attack up to (α) = 19.2°. This is accordingly visualized at the span stations of r/R = 0.63 in Fig. 18 (c-d). It is worth noting that at a wind speed of 3 m/s, the local angles of attack are negative between span stations of $0.25 \leq r/R \leq 0.45$, resulting in negative aerodynamic forces, torque, and thrust as seen in Fig. 13 and Fig. 16.

Table 5: Thrust and Flapwise bending moment of the NREL Phase-VI: Baseline, and MTE blades.

Wind speed, U_w (m/s)	Tip Speed Ratio (λ)	Thrust (N)			Flapwise Bending Moment (N.m)		
		Baseline	MTE	Increment	Baseline	MTE	Increment
3	12.6	69.8	325.8	367 %	277.9	1182.2	325.4 %
5	7.6	305.4	445.4	45.8 %	1062.3	1567.6	47.6 %
7	5.4	544.3	590.9	8.6 %	1842.0	2016.1	9.5 %
9	4.2	749.1	808.9	8.0 %	2499.0	2675.9	7.1 %

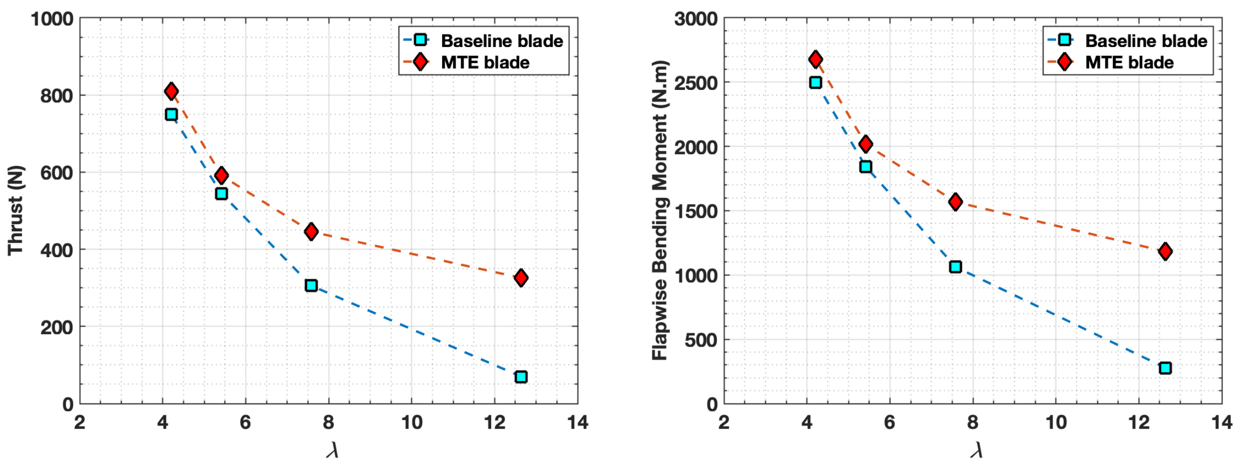

(a) **(b)**

Fig. 15: Comparative analysis of: (a) Thrust, (b) Flapwise bending moment; of NREL Phase-VI: Baseline, and MTE blades.

4.5 Skin Friction and Surface flow

The airflow over wind turbine blades is complex and three-dimensional. The boundary layer dynamics are affected by the centrifugal and Coriolis forces, which drive the inflow radially outward and amplify the chordwise pressure differential, respectively [62]. Skin friction plays a crucial role in subsonic flow regimes, facilitating the transfer of momentum from the inflow to the blade surface, leading to the development of turbulent boundary layers. These layers are characterized by turbulent eddies that decrease the boundary layer thickness, reducing pressure drag on the blade and delaying flow separation. The skin friction contours, and surface flow streamlines are used to investigate the variations in airflow characteristics across the blade surface. The skin friction contours are color-coded and overlapped with surface flow streamlines to indicate variations in the flow pattern. The visualizations in Fig. 20-21 show unsteady flows primarily over the suction surface due to the thick blade profile. These flows originate from the blade root region and increase with wind speed. Skin friction decreases in the chordwise direction due to the loss of kinetic energy and in the spanwise direction due to the increment in local incidence angles (α), which advance flow transition/separation.

At lower wind speeds of 3-7 m/s, the inflow is fully attached to the blade with an unsteady flow pattern developing radially outward from the root with the increment in wind speed, as apparent in Fig. 20 (a-d). The MTE blades significantly increase the skin friction across the blade span at lower wind speeds owing to the strengthening of the boundary layers caused by the increase in mean blade camber. At higher wind speed of 9 m/s, the airflow characteristics exhibit significant alterations depicted in Fig. 21, with unsteady radial flows originating from the blade root and extending across approximately 85% of blade suction surface. It is accompanied by flow-detachment

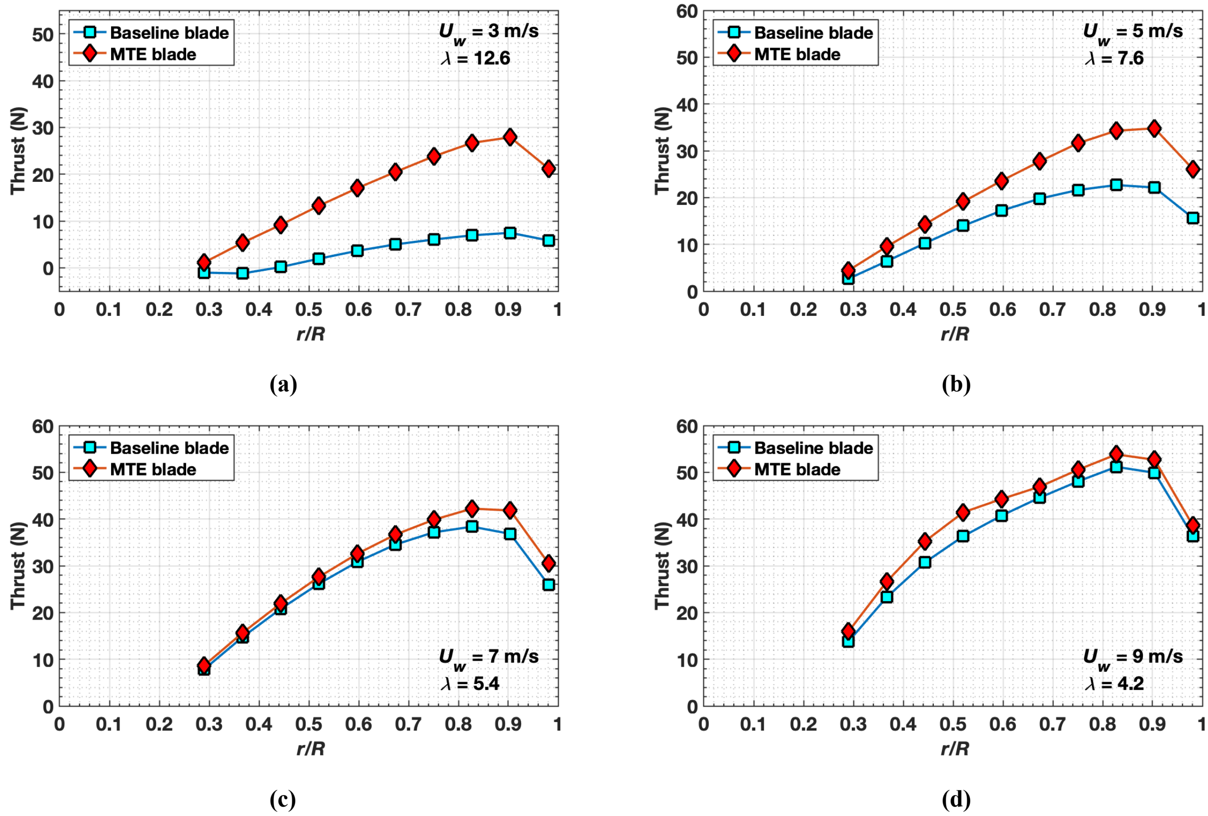

Fig. 16: Spanwise distribution of Thrust of NREL Phase-VI: Baseline, and MTE blades.

over aft-50% blade chord across span stations of $0.35 \leq r/R \leq 0.85$, as detected in Fig. 18 (c-d). The MTE blades exhibit comparatively higher skin friction across the blade span due to the optimized, morphing trailing-edge topology.

4.6 Flow Turbulence

Turbulent kinetic energy (TKE) is a measure of the energy associated with the random motion of fluid particles in a turbulent flow. In laminar flow regimes, small spatial disturbances or perturbations can easily grow and lead to separation. Higher levels of TKE can be beneficial in suppressing flow separation by promoting mixing of the flow. The inherent turbulent eddies and vortices prevent the growth of disturbances and tend to maintain a laminar flow over the surface. TKE is measured for both Baseline and MTE blades subjected to wind speeds ranging from 3-9 m/s (λ = 12.6-4.2). The normalized TKE (TKE/U_w^2) visualization presented in Fig. 22-23 for the trailing-edge region at different span stations shows progressive amplification in the radially outward direction. The exhibition is limited to two cases of U_w = 3, and 9 m/s, for the sake of brevity.

The increment in wind speed further intensifies turbulent kinetic energy, owing to the magnification of local incidence angles (α) across the span. It is accompanied by enlargement and traverse of the turbulent core farther from the trailing-edge, along with considerable wake expansion. The presented contours also exhibit the characteristic double-peak wake, that arise due to the intermixing and subsequent interaction of boundary layers from across the blade surfaces.

The MTE blades exhibit significant increments in TKE compared to the Baseline blade, which is attributed to the acceleration of inflow over the blade suction surface induced by the magnification of the mean blade-camber. The relative amplification in peak-TKE is recorded up to 79%, 40%, 10%, and 20% for wind speeds of 3, 5, 7, and 9

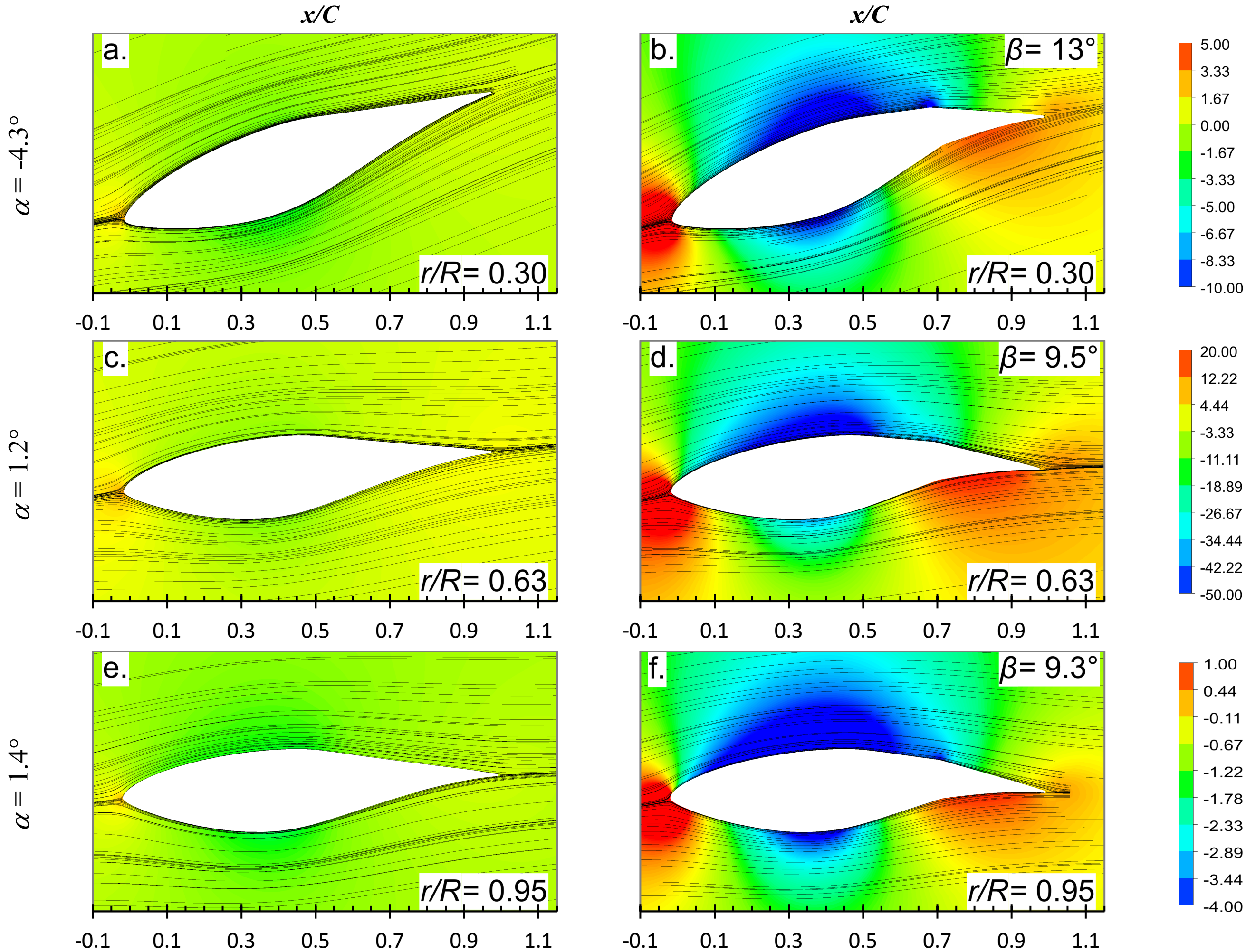

Fig. 17: Pressure coefficient (C_{prs}) contours superimposed with velocity streamlines around the NREL Phase-VI blades: (left) Baseline, and (right) MTE, subjected to wind speed of U_w = 3 m/s, at different span stations.

m/s, respectively. The increased TKE at low wind speeds strengthens the boundary layers and suppresses flow transition. The spike in TKE detected at span stations of $0.47 \leq r/R \leq 0.80$ at a wind speed of 9 m/s in Fig. 23 (c-d), is due to the transition of laminar flow into turbulent flow caused by the separated flow regime detected in Fig. 18 (c-d) and Fig. 21 (a-b).

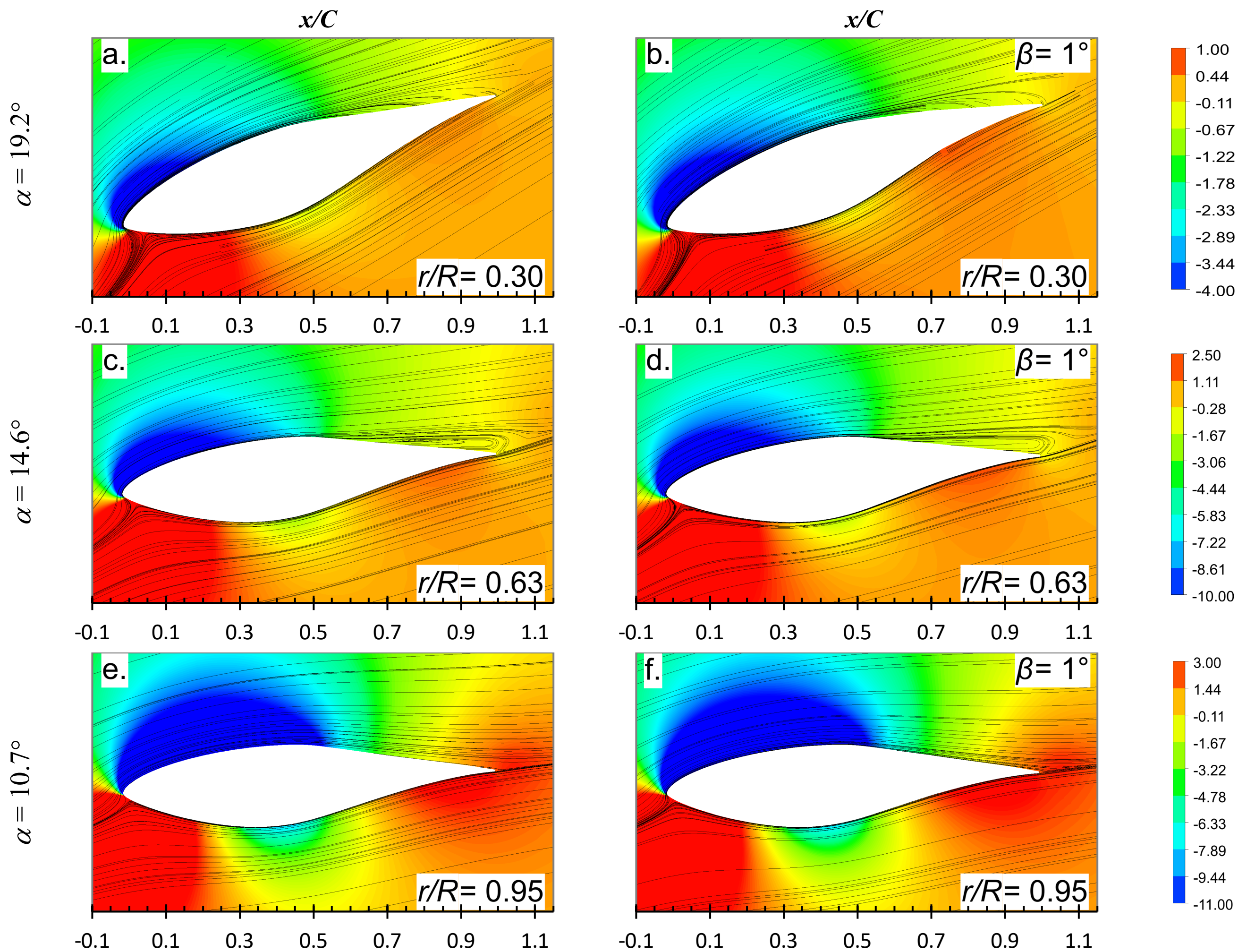

Fig. 18: Pressure coefficient (C_{prs}) contours superimposed with velocity streamlines around the NREL Phase-VI blades: (left) Baseline, and (right) MTE, subjected to wind speed of U_w = 9 m/s, at different span stations.

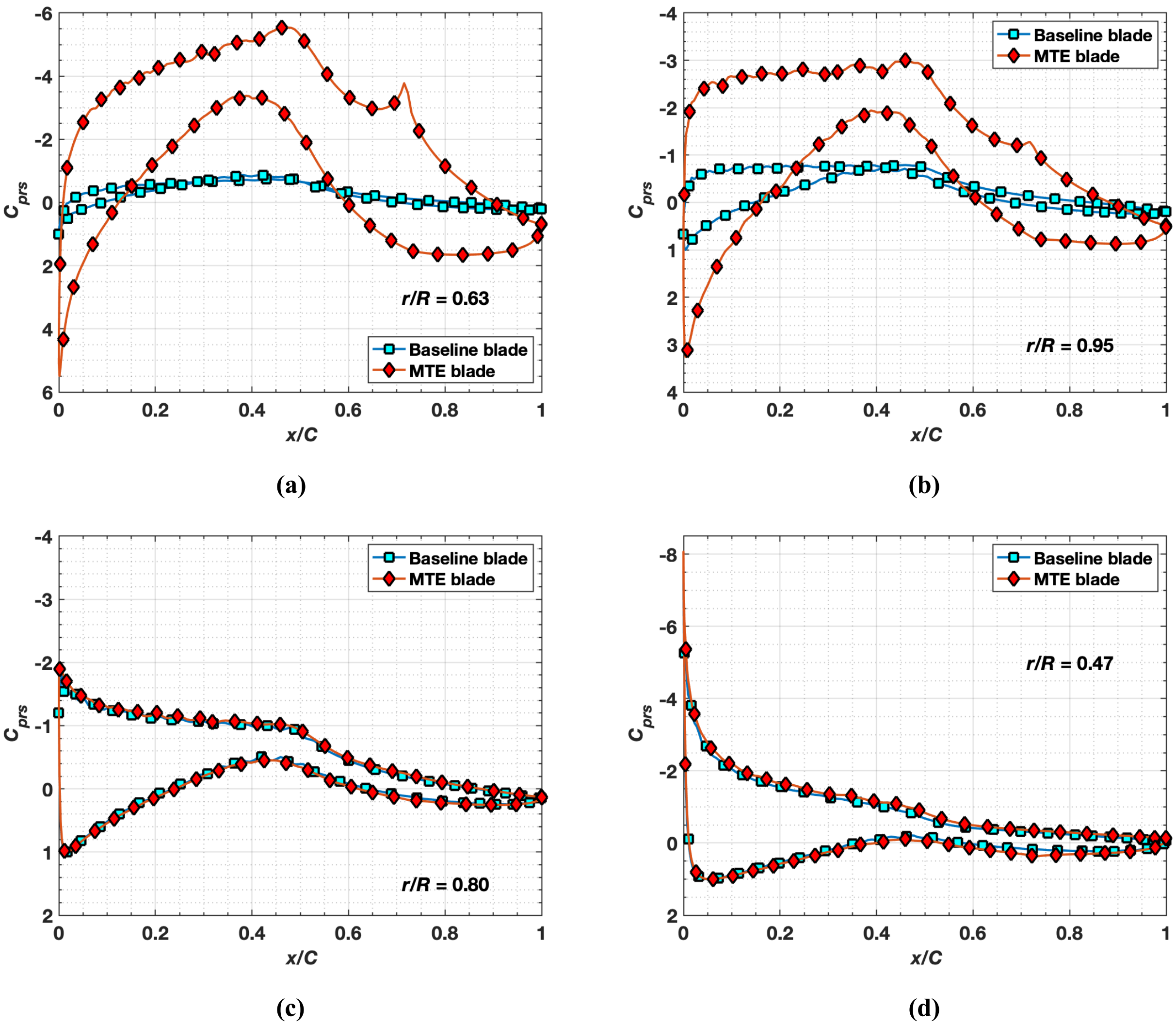

Fig. 19: Pressure coefficient (C_{prs}) distribution around the NREL Phase-VI: Baseline, and MTE blades subjected to wind speeds of: (a-d) 3, 5, 7, and 9 m/s, at different span stations.

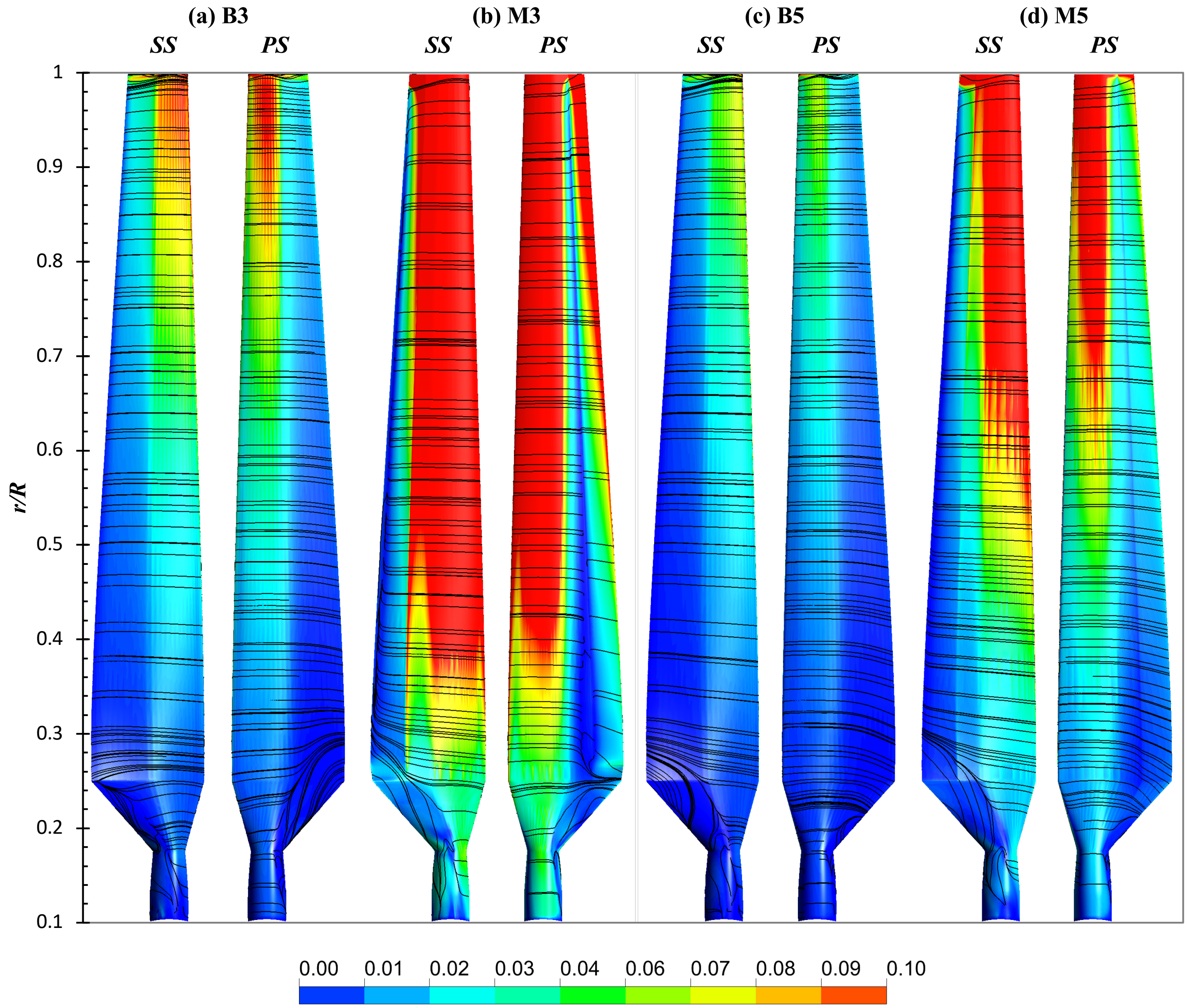

Fig. 20: Skin friction coefficient contours with superimposed surface-flow streamlines on NREL Phase-VI blades: (a & c) Baseline, and (b & d) MTE, subjected to windspeed of U_w = 3 and 5 m/s.

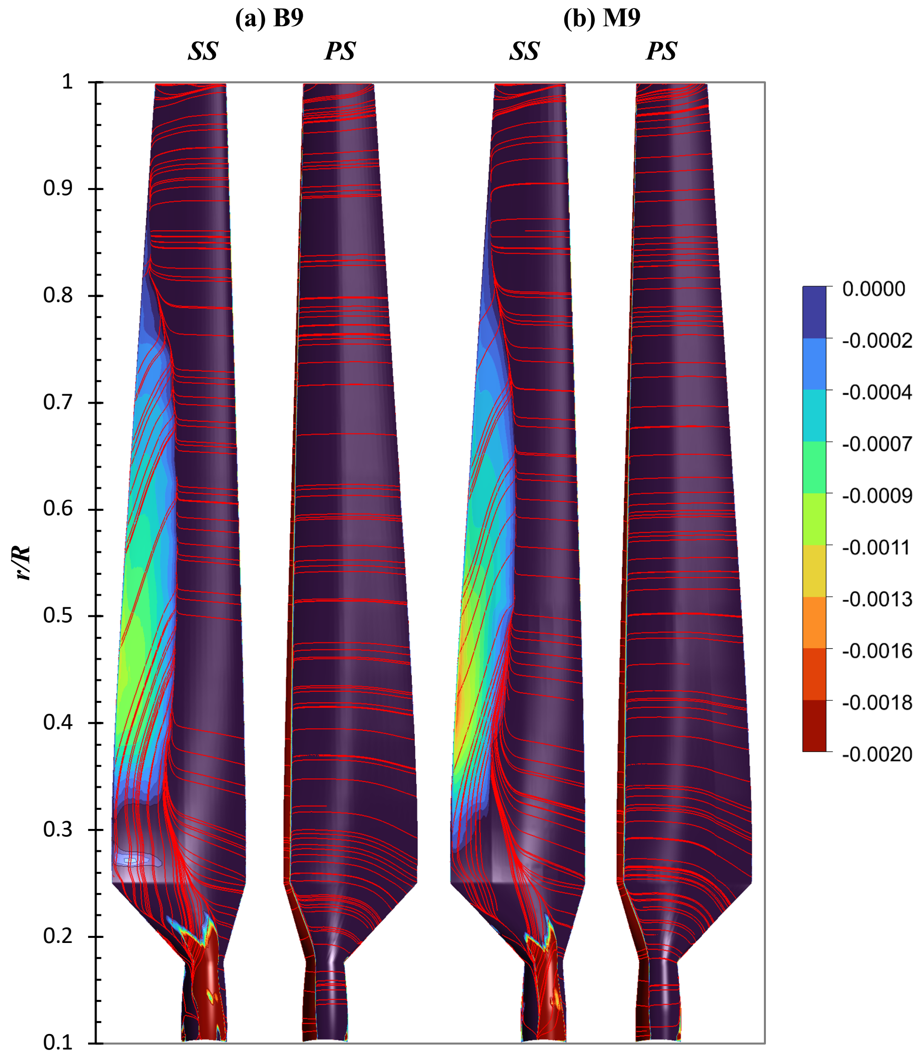

Fig. 21: Skin friction (streamwise) coefficient contours with superimposed surface-flow streamlines on NREL Phase-VI blades: (a) Baseline, and (b) MTE, subjected to windspeed of U_w = 9 m/s.

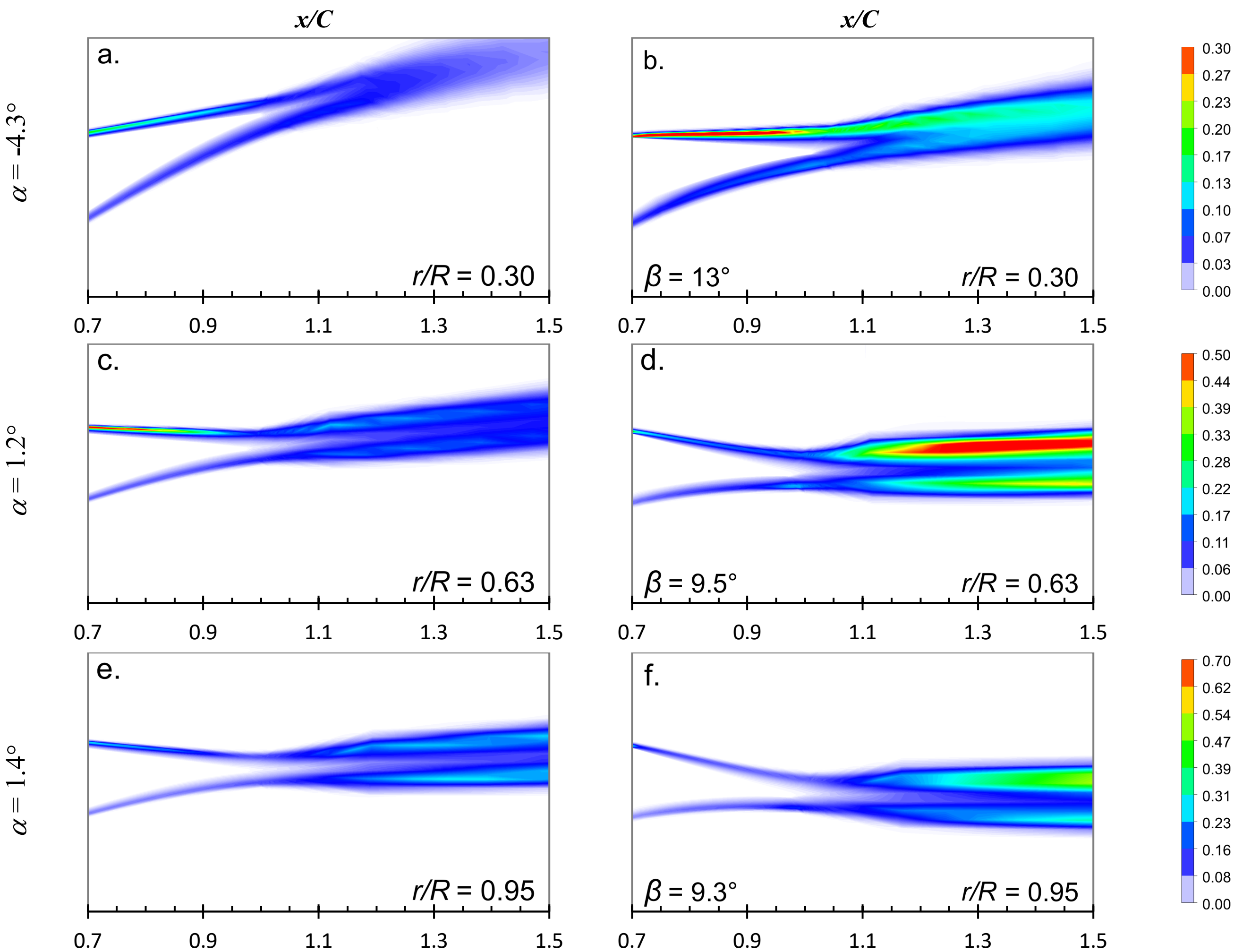

Fig. 22: Normalized Turbulent Kinetic Energy (TKE/U_w^2) contours around the NREL Phase-VI blades: (left) Baseline, and (right) MTE, subjected to wind speed of $U_w = 3$ m/s, at different span stations.

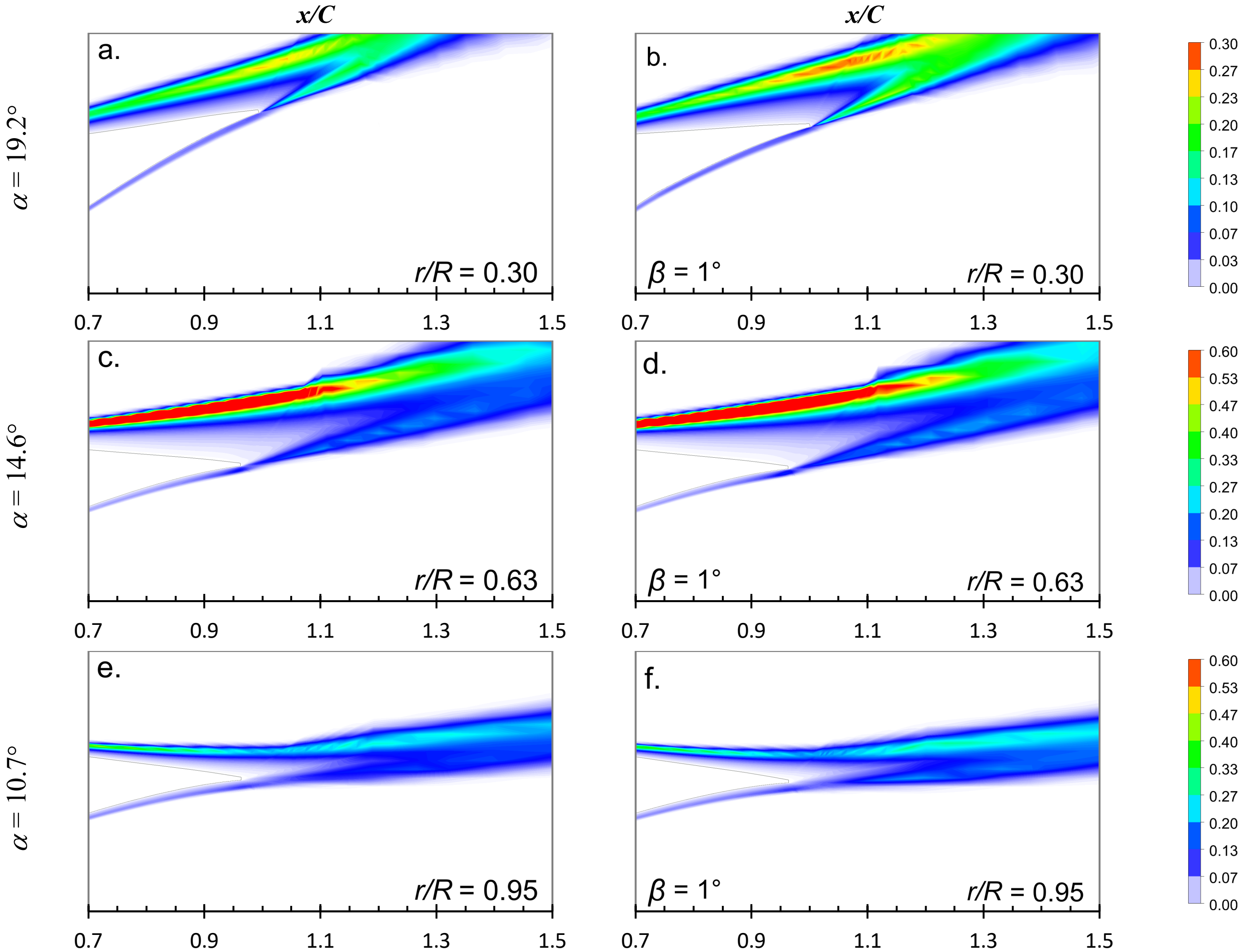

Fig. 23: Normalized Turbulent Kinetic Energy (TKE/U_w^2) contours around the NREL Phase-VI blades: (left) Baseline, and (right) MTE, subjected to wind speed of U_w = 9 m/s, at different span stations.

4.7 Aeroacoustics

The morphing trailing-edge (MTE) wind turbine blades have substantial impact on the aerodynamic noise due to variations in skin friction, turbulent kinetic energy, and wake deficit. These alterations may lead to an increase in turbulent fluctuations and sound radiation, resulting in higher overall noise levels. Factors such as flow separation and turbulent mixing in the wake region also contribute to this phenomenon. Therefore, further research is conducted to characterize the aerodynamic noise generated by MTE and Baseline blades.

4.7.1 Vorticity

The vorticity in wind turbine blades plays a significant role in the generation of aerodynamic noise. Vortex shedding from the trailing-edge of the blade creates a fluctuating pressure field, which generates tonal noise. Vortex breakdown across the blade surface also leads to the generation of broadband noise with a wide frequency range. Additionally, the interaction of vortices with boundary layers results in an increase in the turbulent kinetic energy of the flow, which amplifies the acoustic radiation. The flow-field around the baseline and MTE blades is analyzed using iso-surface plots of velocity magnitude at different wind speeds in Fig. 24. The results indicate that at lower wind speeds, vortex shedding is primarily confined to the trailing-edge region. While in the case of MTE blades, shedding is initiated at the hinge location ($x/C = 0.7$) of the morphing trailing-edge. As wind speed increases, vortex dissipation occurs primarily over the aft-50% of the blade chord, which coincides with the flow transition zones detected in the surface flow and skin friction contours (refer: Fig. 21), as well as the velocity-field measurements (refer to Fig. 18).

4.7.2 Strain rate

Strain rate plays a crucial role in aerodynamic noise generation. High strain rates lead to the formation of turbulent eddies and vortices, which transfer energy to the inflow and create acoustic pressure fluctuations. High strain rates also accelerate the onset of flow transition and separation, altering boundary layer dynamics and increasing turbulent fluctuations and kinetic energy, resulting in higher broadband noise. The normalized instantaneous surface rate of strain [Strain Rate*$\left({c_{tip}}/{U_w}\right)$, where c_{tip} is blade-tip chord length] for blade models is evaluated at different wind speeds and presented for two representative cases of $U_w = 3$ and 9 m/s in Fig. 25. It showcases a strain rate gradient along the blade leading-edge in the radially outward direction. This is due to higher local velocities induced by the blade rotation. The spatial distribution of strain rate over the MTE blades features a larger gradient, resulting from the relatively higher inflow velocities across the surface achieved by the acceleration of inflow over the MTE blades induced by the mean blade camber magnification through trailing-edge morphing. At lower wind speeds, the strain rate contours in Fig. 25 (a-b) exhibit smooth patterns, indicative of laminar flow across the blade surface. While, at higher wind speeds the contours in Fig. 25 (c-d) depict a turbulent flow regime.

4.7.3 Far-field Noise

The acoustic analysis of Baseline and MTE-integrated wind turbine is conducted at the wind speed of 9 m/s. In order to predict the overall noise for the NREL Phase VI wind turbine, which features two blades, an additional identical source is placed at the relative position of the second blade, as proposed in reference [73]. To simplify the analysis, the acoustic sources are considered incoherent, which prevents any noise cancellation effects based on phase differences. The time-averaged approximation of the far-field noise is obtained by evenly placing 36 ground receivers around the wind turbine in a circular plane at a radius of ($H + D/2$).

The noise footprint of the NREL Phase VI wind turbine featuring Baseline and MTE blades is presented in Fig. 26. The Sound Pressure Level (SPL) and Overall Sound Pressure Level (OASPL) are computed across a frequency spectrum of 100 - 20,000 Hz. The SPL of the MTE and Baseline configured wind turbines captured by the receiver placed 17.2 m downwind is presented in Fig. 26 (a). As expected, the wind turbine featuring MTE blades generates higher broadband noise compared to the Baseline counterpart.

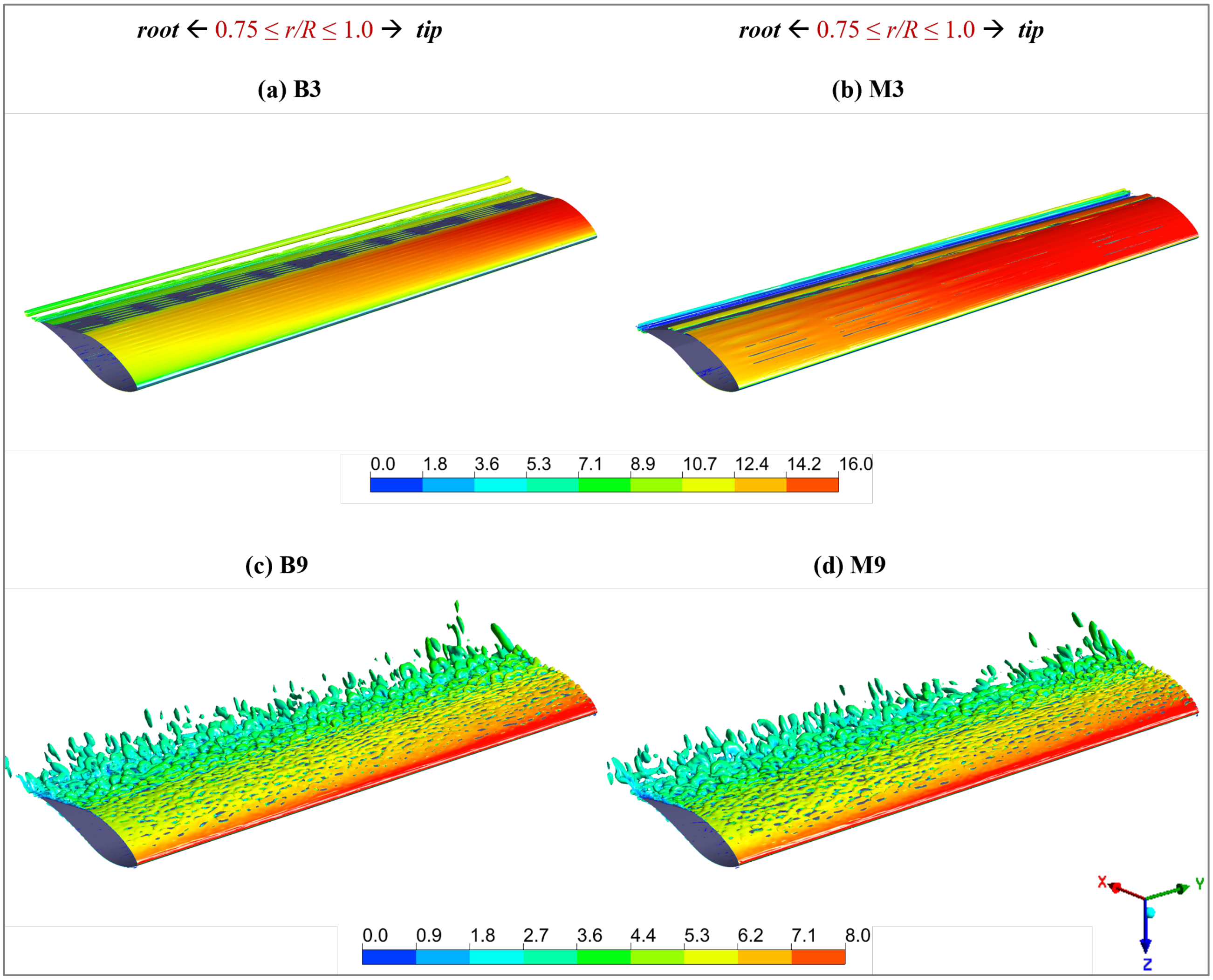

Fig. 24: Instantaneous iso-surface of Q-criterion (Q = 1 x 10^5 s^{-2}) with contours of normalized velocity (U_∞/U_w) for the NREL Phase-VI blades: (a & c) Baseline, and (b & d) MTE, subjected to wind speeds (U_w): (top) 3 m/s, and (bottom) 9 m/s.

This finding corresponds with the comparatively higher skin friction, turbulent kinetic energy, and wake deficit exhibited by the MTE blades. The noise level of the MTE-integrated wind turbine is approximately 10 dB higher than the Baseline over lower frequencies ($f < 500$ Hz). However, this difference progressively reduces and becomes insignificant across higher noise frequencies ($f > 500$ Hz). The computed OASPL plot in Fig. 26 (b) exhibits a dipole pattern with the lowest noise levels in the wind turbine's rotational plane, as reported in the literature [73,74]. The overall noise level in the upwind direction is observed to be marginally higher than the downwind. This is accredited to the Doppler effect induced by the blowing of wind, as previously observed by researchers in [73]. The MTE configured NREL Phase VI wind turbine exhibits a slightly higher overall noise level (0.25 dB) than its Baseline counterpart.

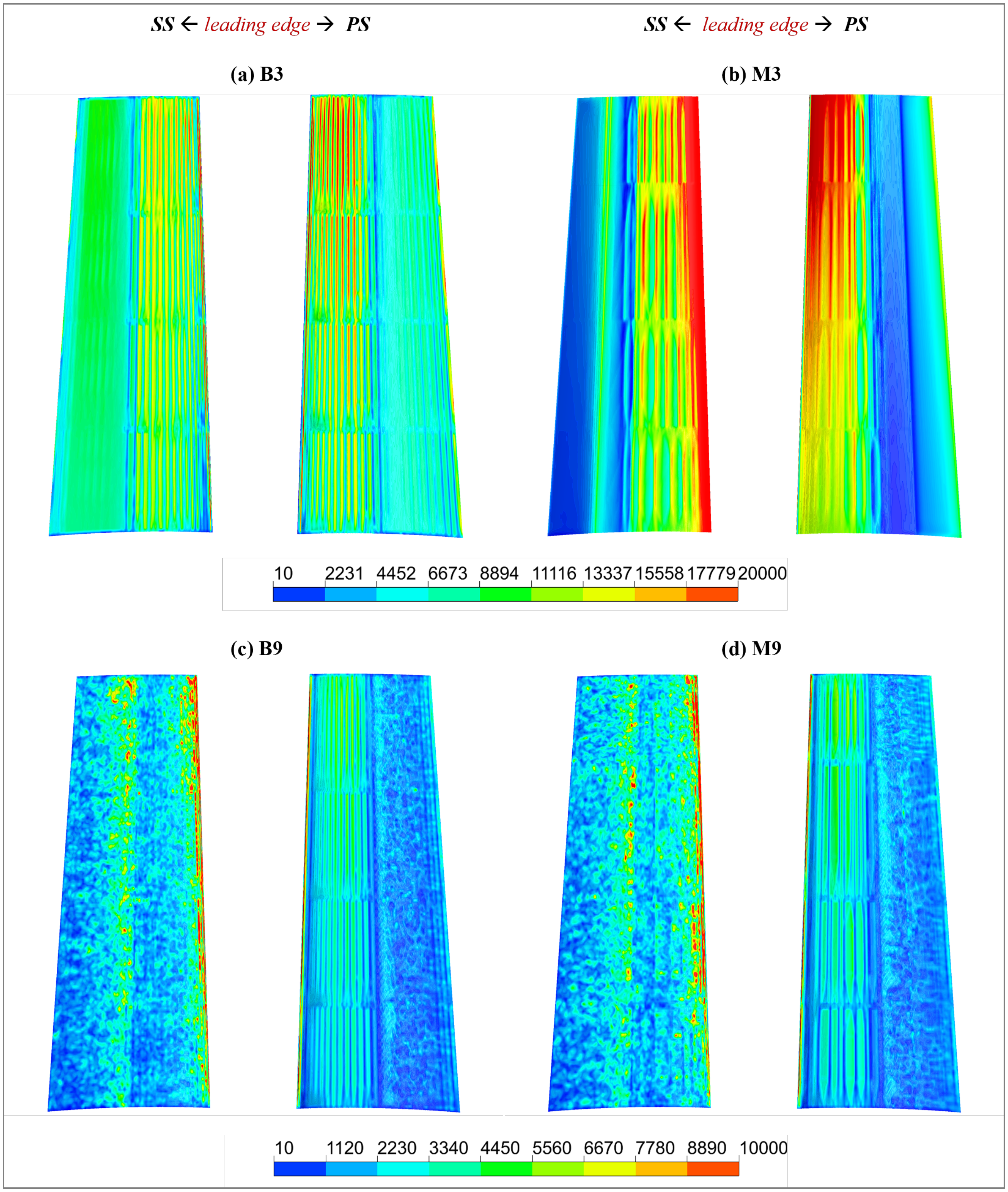

Fig. 25: Normalized Instantaneous surface rate of strain [Strain Rate*$\left({}^{C_{tip}}/_{U_w}\right)$] contours for the NREL Phase-VI blades: (a & c) Baseline, and (b & d) MTE, subjected to windspeed of U_w: (top) 3 m/s, and (bottom) 9 m/s.

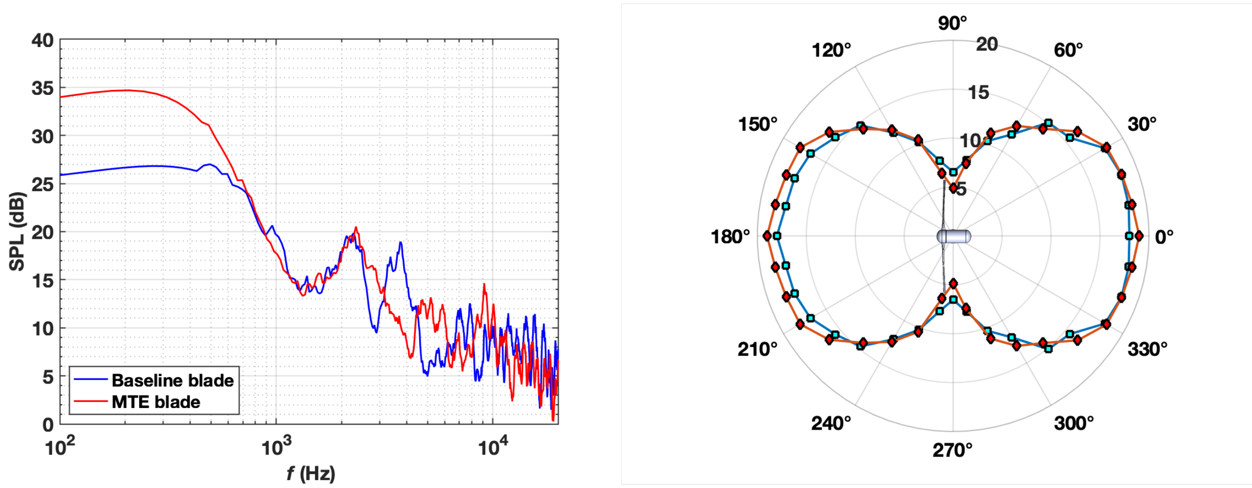

(a) (b)

Fig. 26: (a) Sound Pressure Level (SPL), and (b) Overall Sound Pressure Level (OASPL) of the NREL Phase-VI wind turbine featuring: (–□–) Baseline, and (–◆–) MTE blades, subjected to wind speed of U_w = 9 m/s.

Conclusion

The current research presents the design and implementation of Morphing Trailing-edge (MTE) blades on NREL Phase VI wind turbines, with the aim of investigating the performance of these blades over low to medium wind speeds (3-9 m/s) through high-fidelity unsteady Computational Fluid Dynamics (CFD) analyses. The MTE blades significantly improve performance, yielding 40% reduction in cut-in wind speed with increments in low-speed shaft torque/power (up to 600%), thrust (up to 367%), and bending moment (up to 325%), compared to baseline blade. The improved performance is attributed to the enhancement of pressure field and flow characteristics through the magnification of the mean camber of the blade, generating significant reductions in the pressure coefficient suction peaks (up to 534%). The MTE blades also increase the inherent turbulent kinetic energy of the inflow, producing greater deficit in wake velocity and turbulent kinetic energy compared to baseline blade. The aeroacoustic signature of the MTE-integrated NREL Phase VI wind turbine exhibits a marginal increase in overall sound pressure level of 0.25 decibels at 9 m/s wind speed. These findings demonstrate the superiority of MTE blades over conventional designs and suggest that MTE-integrated wind turbines have potential to promote the use of sustainable energy in off-grid and remote areas. These wind turbines will not only contribute to the United Nations' sustainable development goal of extending the outreach of renewable energy (SDG 7), but also reduce the levelized cost of energy through increased annual energy production.

References

[1] Renewable Energy Agency I. Renewable capacity highlights 2022 2022.

[2] Wright AK, Wood DH. The starting and low wind speed behaviour of a small horizontal axis wind turbine. Journal of Wind Engineering and Industrial Aerodynamics 2004;92:1265–79. https://doi.org/10.1016/J.JWEIA.2004.08.003.

[3] Simic Z, Havelka JG, Bozicevic Vrhovcak M. Small wind turbines – A unique segment of the wind power market. Renew Energy 2013;50:1027–36. https://doi.org/10.1016/J.RENENE.2012.08.038.

[4] Giguère P, Selig MS. Low Reynolds number airfoils for small horizontal axis wind turbines. Wind Engineering 1997;21:367–80.

[5] Leung DYC, Deng Y, Leung MKH. Design Optimization of a Cost-Effective Micro Wind Turbine. Proceedings of the World Congress on Engineering (WCE-2010), London: 2010.

[6] IEA, IRENA, UNSD, World Bank, WHO. Tracking SDG 7: The Energy Progress Report. Washington DC: 2022.

[7] Tummala A, Velamati RK, Sinha DK, Indraja V, Krishna VH. A review on small scale wind turbines. Renewable and Sustainable Energy Reviews 2016;56:1351–71. https://doi.org/10.1016/J.RSER.2015.12.027.

[8] Hansen MOL. Aerodynamics of wind turbines: Third edition. Aerodynamics of Wind Turbines: Third Edition 2015:1–173. https://doi.org/10.4324/9781315769981.

[9] Jureczko M, Pawlak M, Mężyk A. Optimisation of wind turbine blades. J Mater Process Technol 2005;167:463–71. https://doi.org/10.1016/J.JMATPROTEC.2005.06.055.

[10] Barlas TK, van Kuik GAM. Review of state of the art in smart rotor control research for wind turbines. Progress in Aerospace Sciences 2010;46:1–27. https://doi.org/10.1016/J.PAEROSCI.2009.08.002.

[11] Zhao Z, Jiang R, Feng J, Liu H, Wang T, Shen W, et al. Researches on vortex generators applied to wind turbines: A review. Ocean Engineering 2022;253:111266. https://doi.org/10.1016/J.OCEANENG.2022.111266.

[12] Garcia-Ribeiro D, Flores-Mezarina JA, Bravo-Mosquera PD, Cerón-Muñoz HD. Parametric CFD analysis of the taper ratio effects of a winglet on the performance of a Horizontal Axis Wind Turbine. Sustainable Energy Technologies and Assessments 2021;47:101489. https://doi.org/10.1016/J.SETA.2021.101489.

[13] Kamliya Jawahar H, Theunissen R, Azarpeyvand M, Ilário da Silva CR. Flow characteristics of slat cove fillers. Aerosp Sci Technol 2020;100:105789. https://doi.org/10.1016/J.AST.2020.105789.

[14] Kamliya Jawahar H, Alihan Showkat Ali S, Azarpeyvand M, Ilário da Silva CR. Aerodynamic and aeroacoustic performance of high-lift airfoil fitted with slat cove fillers. J Sound Vib 2020;479:115347. https://doi.org/10.1016/J.JSV.2020.115347.

[15] Kamliya Jawahar H, Showkat Ali SA, Azarpeyvand M. Aeroacoustic characteristics of slat finlets. Physics of Fluids 2021;33:097102. https://doi.org/10.1063/5.0061367.

[16] Zaki A, Abdelrahman MA, Ayad SS, Abdellatif OE. Effects of leading edge slat on the aerodynamic performance of low Reynolds number horizontal axis wind turbine. Energy 2022;239:122338. https://doi.org/10.1016/J.ENERGY.2021.122338.

[17] Chamorro LP, Arndt REA, Sotiropoulos F. Drag reduction of large wind turbine blades through riblets: Evaluation of riblet geometry and application strategies. Renew Energy 2013;50:1095–105. https://doi.org/10.1016/J.RENENE.2012.09.001.

[18] Özkan M, Erkan O. Control of a boundary layer over a wind turbine blade using distributed passive roughness. Renew Energy 2022;184:421–9. https://doi.org/10.1016/J.RENENE.2021.11.082.

[19] Sedighi H, Akbarzadeh P, Salavatipour A. Aerodynamic performance enhancement of horizontal axis wind turbines by dimples on blades: Numerical investigation. Energy 2020;195:117056. https://doi.org/10.1016/J.ENERGY.2020.117056.

[20] Aubrun S, Leroy A, Devinant P. A review of wind turbine-oriented active flow control strategies. Exp Fluids 2017;58:1–21. https://doi.org/10.1007/S00348-017-2412-0/TABLES/1.

[21] Ye X, Hu J, Zheng N, Li C. Numerical study on aerodynamic performance and noise of wind turbine airfoils with serrated gurney flap. Energy 2023;262:125574. https://doi.org/10.1016/J.ENERGY.2022.125574.

[22] Lee JW, Han JH, Shin HK, Bang HJ. Active load control of wind turbine blade section with trailing edge flap: Wind tunnel testing. Http://DxDoiOrg/101177/1045389X14544143 2014;25:2246–55. https://doi.org/10.1177/1045389X14544143.

[23] Castaignet D, Barlas T, Buhl T, Poulsen NK, Wedel-Heinen JJ, Olesen NA, et al. Full-scale test of trailing edge flaps on a Vestas V27 wind turbine: Active load reduction and system identification. Wind Energy 2014;17:549–64. https://doi.org/10.1002/WE.1589.

[24] Plumley C, Leithead W, Jamieson P, Bossanyi E, Graham M. Comparison of individual pitch and smart rotor control strategies for load reduction. J Phys Conf Ser 2014;524:012054. https://doi.org/10.1088/1742-6596/524/1/012054.

[25] Ng BF, Palacios R, Kerrigan EC, Graham JMR, Hesse H. Aerodynamic load control in horizontal axis wind turbines with combined aeroelastic tailoring and trailing-edge flaps. Wind Energy 2016;19:243–63. https://doi.org/10.1002/WE.1830.

[26] Lackner MA, van Kuik G. A comparison of smart rotor control approaches using trailing edge flaps and individual pitch control. Wind Energy 2010;13:117–34. https://doi.org/10.1002/WE.353.

[27] Fischer A, Madsen HA. Investigation of the theoretical load alleviation potential using trailing edge flaps controlled by inflow data. Wind Energy 2016;19:1567–83. https://doi.org/10.1002/WE.1937.

[28] Oltmann NC, Sobotta D, Hoffmann A. Load reduction of wind turbines using trailing edge flaps. Energy Procedia 2017;136:176–81. https://doi.org/10.1016/J.EGYPRO.2017.10.316.

[29] Smit J, Bernhammer LO, Navalkar ST, Bergami L, Gaunaa M. Sizing and control of trailing edge flaps on a smart rotor for maximum power generation in low fatigue wind regimes. Wind Energy 2016;19:607–24. https://doi.org/10.1002/WE.1853.

[30] Chen ZJ, Stol KA, Mace BR. Wind turbine blade optimisation with individual pitch and trailing edge flap control. Renew Energy 2017;103:750–65. https://doi.org/10.1016/J.RENENE.2016.11.009.

[31] Omidi J, Mazaheri K. Aerodynamic Enhancement and Improving the Performance of a Six-Megawatt DOWEC Wind Turbine by Micro-Plasma Actuator. Int J Mech Sci 2021;195:106228. https://doi.org/10.1016/J.IJMECSCI.2020.106228.

[32] Wang L, Alam MM, Rehman S, Zhou Y. Effects of blowing and suction jets on the aerodynamic performance of wind turbine airfoil. Renew Energy 2022;196:52–64. https://doi.org/10.1016/J.RENENE.2022.06.126.

[33] Lachenal X, Daynes S, Weaver PM. Review of morphing concepts and materials for wind turbine blade applications. Wind Energy 2013;16:283–307. https://doi.org/10.1002/WE.531.

[34] Kamliya Jawahar H. Aerodynamic and Aeroacoustic Performance of Morphing Structures. Fluid and Aerodynamics. University of Bristol, 2019.

[35] Kamliya Jawahar H, Ai Q, Azarpeyvand M. Experimental and numerical investigation of aerodynamic performance for airfoils with morphed trailing edges. Renew Energy 2018;127:355–67. https://doi.org/10.1016/J.RENENE.2018.04.066.

[36] Kamliya Jawahar H, Vemuri SS, Azarpeyvand M. Aerodynamic noise characteristics of airfoils with morphed trailing edges. Int J Heat Fluid Flow 2022;93:108892. https://doi.org/10.1016/J.IJHEATFLUIDFLOW.2021.108892.

[37] Kamliya Jawahar H, Azarpeyvand M, Ilário da Silva CR. Acoustic and flow characteristics of an airfoil fitted with morphed trailing edges. Exp Therm Fluid Sci 2021;123:110287. https://doi.org/10.1016/J.EXPTHERMFLUSCI.2020.110287.

[38] Akhter MZ, Omar FK, Ali AR. Self-adaptive Variable Twist Morphing Blade for Wind Turbine. US 11,448,184 B1, 2022.

[39] Abbott IH, von Doenhoff AE. Theory of Wing Sections: Including a Summary of Airfoil Data. Dover Publications; 1959.

[40] Thill C, Etches J, Bond I, Potter K, Weaver P. Morphing skins. The Aeronautical Journal 2008;112:117–39. https://doi.org/10.1017/S0001924000002062.

[41] Sofla AYN, Meguid SA, Tan KT, Yeo WK. Shape morphing of aircraft wing: Status and challenges. Mater Des 2010;31:1284–92. https://doi.org/10.1016/J.MATDES.2009.09.011.

[42] Barbarino S, Bilgen O, Ajaj RM, Friswell MI, Inman DJ. A Review of Morphing Aircraft. J Intell Mater Syst Struct 2011;22:823–77. https://doi.org/10.1177/1045389X11414084.

[43] Akhter MZ, Omar FK. Review of Flow-Control Devices for Wind-Turbine Performance Enhancement. Energies 2021, Vol 14, Page 1268 2021;14:1268. https://doi.org/10.3390/EN14051268.

[44] Straub FK. A feasibility study of using smart materials for rotor control. Smart Mater Struct 1996;5:1. https://doi.org/10.1088/0964-1726/5/1/002.

[45] Chopra I. Review of State of Art of Smart Structures and Integrated Systems. Https://DoiOrg/102514/21561 2012;40:2145–87. https://doi.org/10.2514/2.1561.

[46] Daynes S, Weaver PM. A morphing trailing edge device for a wind turbine. Http://DxDoiOrg/101177/1045389X12438622 2012;23:691–701. https://doi.org/10.1177/1045389X12438622.

[47] Daynes S, Weaver PM. Design and testing of a deformable wind turbine blade control surface. Smart Mater Struct 2012;21:105019. https://doi.org/10.1088/0964-1726/21/10/105019.

[48] Bak C, Gaunaa M, Andersen PB, Buhl T, Hansen P, Clemmensen K, et al. Wind tunnel test on wind turbine airfoil with adaptive trailing edge geometry. Collection of Technical Papers - 45th AIAA Aerospace Sciences Meeting 2007;18:12314–25. https://doi.org/10.2514/6.2007-1016.

[49] Troldborg N. Computational Study of the Risø-B1-18 Airfoil with a Hinged Flap Providing Variable Trailing Edge Geometry. Http://DxDoiOrg/101260/0309524054797159 2016;29:89–113. https://doi.org/10.1260/0309524054797159.

[50] Barlas TK, van Kuik GAM. State of the art and prospectives of smart rotor control for wind turbines. J Phys Conf Ser 2007;75:012080. https://doi.org/10.1088/1742-6596/75/1/012080.

[51] van Wingerden JW, Hulskamp AW, Barlas T, Marrant B, van Kuik GAM, Molenaar DP, et al. On the proof of concept of a 'Smart' wind turbine rotor blade for load alleviation. Wind Energy 2008;11:265–80. https://doi.org/10.1002/WE.264.

[52] Cairns DS, Blockey JC, Ehresman J. Design and feasibility of active control surfaces on wind turbine blade systems. 46th AIAA Aerospace Sciences Meeting and Exhibit 2008. https://doi.org/10.2514/6.2008-1341.

[53] Pechlivanoglou GK, Wagner J, Nayeri CN, Paschereit CO. Active aerodynamic control of wind turbine blades with high deflection flexible flaps. 48th AIAA Aerospace Sciences Meeting Including the New Horizons Forum and Aerospace Exposition 2010. https://doi.org/10.2514/6.2010-644.

[54] Bergami L, Poulsen NK. A smart rotor configuration with linear quadratic control of adaptive trailing edge flaps for active load alleviation. Wind Energy 2015;18:625–41. https://doi.org/10.1002/WE.1716.

[55] Bernhammer LO, van Kuik GAM, de Breuker R. Fatigue and extreme load reduction of wind turbine components using smart rotors. Journal of Wind Engineering and Industrial Aerodynamics 2016;154:84–95. https://doi.org/10.1016/J.JWEIA.2016.04.001.

[56] Akhter MZ, Riyadh Ali A, Omar FK. Wind Turbine Power Augmentation Using Virtually Morphed Trailing Edge. 2021 6th International Conference on Renewable Energy: Generation and Applications, ICREGA 2021, Institute of Electrical and Electronics Engineers Inc.; 2021, p. 233–6. https://doi.org/10.1109/ICREGA50506.2021.9388308.

[57] Akhter MZ, Ali AR, Omar FK. Design and Analysis of a Morphing Trailing Edge System. 2021 6th International Conference on Renewable Energy: Generation and Applications, ICREGA 2021, Institute of Electrical and Electronics Engineers Inc.; 2021, p. 58–62. https://doi.org/10.1109/ICREGA50506.2021.9388221.

[58] Ali AR, Akhter MZ, Omar FK. Performance enhancement of a small-scale wind turbine featuring morphed trailing edge. Sustainable Energy Technologies and Assessments 2021;46:101229. https://doi.org/10.1016/J.SETA.2021.101229.

[59] Hand MM, Simms DA, Fingersh LJ, Jager DW, Cotrell JR, Schreck S, et al. Unsteady Aerodynamics Experiment Phase VI: Wind Tunnel Test Configurations and Available Data Campaigns 2001. https://doi.org/10.2172/15000240.

[60] Jawahar HK, Ai Q, Azarpeyvand M. Experimental and numerical investigation of aerodynamic performance of airfoils fitted with morphing trailing-edges. 23rd AIAA/CEAS Aeroacoustics Conference, 2017 2017. https://doi.org/10.2514/6.2017-3371.

[61] Akhter MZ, Ali AR, Omar FK. Aerodynamics of a three-dimensional bionic morphing flap. Sustainable Energy Technologies and Assessments 2022;52. https://doi.org/10.1016/J.SETA.2022.102286.

[62] Lomax H, Pulliam TH, Zingg DW. Fundamentals of Computational Fluid Dynamics 2001. https://doi.org/10.1007/978-3-662-04654-8.

[63] Menter FR, Langtry R, Völker S. Transition Modelling for General Purpose CFD Codes. Flow, Turbulence and Combustion 2006 77:1 2006;77:277–303. https://doi.org/10.1007/S10494-006-9047-1.

[64] Benjanirat S, Sankar LN, Xu G. Evaluation of turbulence models for the prediction of wind turbine aerodynamics. ASME 2003 Wind Energy Symposium, WIND2003 2003:73–83. https://doi.org/10.1115/WIND2003-517.

[65] Tachos NS, Filios AE, Margaris DP. A comparative numerical study of four turbulence models for the prediction of horizontal axis wind turbine flow. Proc Inst Mech Eng C J Mech Eng Sci 2010;224:1973–9. https://doi.org/10.1243/09544062JMES1901.

[66] Moshfeghi M, Song YJ, Xie YH. Effects of near-wall grid spacing on SST-K-ω model using NREL Phase VI horizontal axis wind turbine. Journal of Wind Engineering and Industrial Aerodynamics 2012;107–108:94–105. https://doi.org/10.1016/J.JWEIA.2012.03.032.

[67] Lanzafame R, Mauro S, Messina M. Wind turbine CFD modeling using a correlation-based transitional model. Renew Energy 2013;52:31–9. https://doi.org/10.1016/J.RENENE.2012.10.007.

[68] Moshfeghi M, Shams S, Hur N. Aerodynamic performance enhancement analysis of horizontal axis wind turbines using a passive flow control method via split blade. Journal of Wind Engineering and Industrial Aerodynamics 2017;167:148–59. https://doi.org/10.1016/J.JWEIA.2017.04.001.

[69] Moshfeghi M, Hur N. Power generation enhancement in a horizontal axis wind turbine blade using split blades. Journal of Wind Engineering and Industrial Aerodynamics 2020;206:104352. https://doi.org/10.1016/J.JWEIA.2020.104352.

[70] Javaherchi T, Antheaume S, Aliseda A. Hierarchical Methodology for the Numerical Simulation of the Flow Field around and in the Wake of Horizontal Axis Wind Turbines: Rotating Reference Frame, Blade Element Method and Actuator Disk Model. Http://DxDoiOrg/101260/0309-524X382181 2014;38:181–202. https://doi.org/10.1260/0309-524X.38.2.181.

[71] Chen ZJ, Przekwas AJ. A coupled pressure-based computational method for incompressible/compressible flows. J Comput Phys 2010;229:9150–65. https://doi.org/10.1016/J.JCP.2010.08.029.

[72] Oerlemans S, Schepers J, Guidati G, Wagner S. Experimental demonstration of wind turbine noise reduction through optimized airfoil noise reduction through optimized airfoil shape and trailing-edge serrations. Copenhagen: 2001.

[73] Wasala SH, Storey RC, Norris SE, Cater JE. Aeroacoustic noise prediction for wind turbines using Large Eddy Simulation. Journal of Wind Engineering and Industrial Aerodynamics 2015;145:17–29. https://doi.org/10.1016/J.JWEIA.2015.05.011.

[74] Moriarty PJ. Development and validation of a semi-empirical wind turbine aeroacoustic code. Collection of ASME Wind Energy Symposium Technical Papers AIAA Aerospace Sciences Meeting and Exhibit 2004:577–86. https://doi.org/10.2514/6.2004-1189.